Remote Sensing of Environment 210 (2018) 387–402

Contents lists available at ScienceDirect

Remote Sensing of Environment

journal homepage: www.elsevier.com/locate/rse

Field-scale mapping of evaporative stress indicators of crop yield: An application over Mead, NE, USA

Yang Yang[a,*], Martha C. Anderson[a], Feng Gao[a], Brian Wardlow[b], Christopher R. Hain[c], Jason A. Otkin[d], Joseph Alfieri[a], Yun Yang[a], Liang Sun[a], Wayne Dulaney[a]

[a] USDA ARS, Hydrology and Remote Sensing Laboratory, Beltsville, MD, USA
[b] School of Natural Resources, University of Nebraska-Lincoln, NE, USA
[c] Marshall Space Flight Center, Earth Science Branch, Huntsville, AL, USA
[d] Space Science and Engineering Center, Cooperative Institute for Meteorological Satellite Studies, University of Wisconsin-Madison, USA

ARTICLE INFO

Keywords:
Evaporative Stress Index (ESI)
Evapotranspiration (ET)
Yield
Landsat
Data fusion

ABSTRACT

The Evaporative Stress Index (ESI) quantifies temporal anomalies in a normalized evapotranspiration (ET) metric describing the ratio of actual-to-reference ET (f_{REF}) as derived from satellite remote sensing. At regional scales (3–10 km pixel resolution), the ESI has demonstrated the capacity to capture developing crop stress and impacts on regional yield variability in water-limited agricultural regions. However, its performance in some regions where the vegetation cycle is intensively managed appears to be degraded due to spatial and temporal limitations in the standard ESI products. In this study, we investigated potential improvements to ESI by generating maps of ET, f_{REF}, and f_{REF} anomalies at high spatiotemporal resolution (30-m pixels, daily time steps) using a multi-sensor data fusion method, enabling separation of landcover types with different phenologies and resilience to drought. The study was conducted for the period 2010–2014 covering a region around Mead, Nebraska that includes both rainfed and irrigated crops. Correlations between ESI and measurements of maize yield were investigated at both the field and county level to assess the potential of ESI as a yield forecasting tool. To examine the role of crop phenology in yield-ESI correlations, annual input f_{REF} time series were aligned by both calendar day and by biophysically relevant dates (e.g. days since planting or emergence). At the resolution of the operational U.S. ESI product (4 km), adjusting f_{REF} alignment to a regionally reported emergence date prior to anomaly computation improves r^2 correlations with county-level yield estimates from 0.28 to 0.80. At 30-m resolution, where pure maize pixels can be isolated from other crops and landcover types, county-level yield correlations improved from 0.47 to 0.93 when aligning f_{REF} by emergence date rather than calendar date. Peak correlations occurred 68 days after emergence, corresponding to the silking stage for maize when grain development is particularly sensitive to soil moisture deficiencies. The results of this study demonstrate the utility of remotely sensed ET in conveying spatially and temporally explicit water stress information to yield prediction and crop simulation models.

1. Introduction

In agricultural regions, water is one of the most widely limiting factors of crop performance and production (Hsiao et al., 1976; Steduto et al., 2012). Indices that describe soil moisture conditions are therefore an integral part of any spatially distributed crop modeling or yield estimation effort. In many crop models, soil moisture constraints are formulated in terms of their impacts on evapotranspiration (ET). ET includes both crop water use through transpiration and water lost through direct soil evaporation, making it a good indicator of soil moisture availability and vegetation health. The value of ET in yield estimation has long been appreciated by agronomists. Jensen (1968) related ET to crop yield through the ratio of actual-to-reference ET, referred to here as f_{REF} but also known in agronomy as the "crop coefficient". This ratio reflects the seasonally changing balance between crop available soil water and the atmospheric demand for water vapor. The milestone publication of Doorenbos and Kassam (1979) established relationships between relative yield losses and reduction in evapotranspiration from potential levels.

Remote sensing offers a unique opportunity to obtain spatially distributed estimates of f_{REF} time evolution over the growing season. In particular, remote sensing algorithms based on surface energy balance

* Corresponding author at: 10300 Baltimore Ave, Beltsville, MD 20705, USA.
E-mail addresses: yang.yang@ars.usda.gov, yangyangwisc@gmail.com (Y. Yang).

https://doi.org/10.1016/j.rse.2018.02.020
Received 12 June 2017; Received in revised form 16 January 2018; Accepted 14 February 2018

have greatly advanced over the past two decades (Kalma et al., 2008; Kustas and Anderson, 2009; Wang and Dickinson, 2012), providing a diagnostic assessment of ET based primarily on thermal infrared (TIR) retrievals of land-surface temperature (LST). Several workable approaches have been developed including the Surface Energy Balance Algorithm for Land (SEBAL; Bastiaanssen et al., 1998), the Mapping Evapotranspiration with Internalized Calibration (METRIC; Allen et al., 2007), the Two Source Energy Balance model (TSEB; Norman et al., 1995), and the Atmosphere–Land Exchange Inverse model (ALEXI; Anderson et al., 1997, 2007a) and an associated disaggregation algorithm (DisALEXI; Anderson et al., 2004). These TIR-based ET mapping algorithms provide regional and global coverage efficiently and economically, motivating studies relating remote sensing-based ET estimates to crop productivity (Bastiaanssen and Ali, 2003; Mishra et al., 2013; Tadesse et al., 2015; Anderson et al., 2016a, 2016b; Mladenova et al., 2017).

Anderson et al. (2007a) proposed the Evaporative Stress Index (ESI) as a new remote sensing drought indicator, which is based on temporal anomalies in f_{RET} retrieved using TIR imagery from geostationary (GEO) satellites. GEO platforms provide both wide-scale spatial coverage and excellent temporal sampling (< 15 min), both advantageous for regional detection of rapid stress onset. The ESI has been shown to agree well with other drought indicators like the U.S. Drought Monitor (USDM) and Standardized Precipitation Index (SPI), but can be developed at significantly higher spatial resolution - constrained primarily by the resolution of the TIR inputs (Anderson et al., 2011, 2013). The ESI also has capabilities for early warning of rapid drought onset (or "flash drought") events (Otkin et al., 2018), conveyed by thermal signals of elevated canopy and soil temperatures that precede visible degradation in the vegetation canopy (Otkin et al., 2013, 2014; Anderson et al., 2011, 2013). Correlations between ESI and reported crop yields have been investigated in the U.S. (Otkin et al., 2016; Mladenova et al., 2017), Brazil (Anderson et al., 2016a), and the Czech Republic (Anderson et al., 2016b), demonstrating capacity to explain regional yield variability in water limited crop growing regions, in many cases providing higher correlations than vegetation index or precipitation anomalies.

While these studies have established the utility of the GEO-based ESI for drought monitoring and yield estimation at regional scales, its performance in some regions where the vegetation cycle is intensively managed appears to be degraded (Anderson et al., 2013). In these areas, anomalies in f_{RET} time series aligned by calendar date are likely confounded by interannual changes in crop phenology, such as variable planting or emergence date, and are therefore less tightly coupled to soil moisture conditions. The impact of variable phenology is manifested in the heart of the U.S. Corn Belt as a reduced correlation between ESI and other drought indicators (Anderson et al., 2013) and with yield (Mladenova et al., 2017).

Degradation in performance in these regions may also be related to the spatial resolution of the remote sensing data used. To date, standard ESI products have had resolutions of 3–10 km, limited by the resolution of the thermal imagery available from geostationary platforms. In heterogeneous agricultural landscapes, however, more drought resilient land cover types such as forest patches, wetlands, and small surface water bodies occurring at the subpixel level may tend to mask the drought response of croplands (Anderson et al., 2015, 2016a). Even pure agricultural pixels may incorporate a mixture of multiple crops with different phenological cycles.

Finally, the sensitivity of crops to soil moisture deficiencies and other environmental stresses varies throughout the growing season, as well as from crop to crop (NeSmith and Ritchie, 1992; McMaster, 2004; Nellis et al., 2009). For example, moisture stress occurring during sensitive stages of corn development, such as emergence, pollination, or grain filling, may reduce the final yield to varying degrees (Wilson, 1968; Claasen and Shaw, 1970; Cakir, 2004; Mkhabela et al., 2010). In order to more reliably relate these stresses to final yields in a remote-sensing based forecasting tool, it is important that individual crop types can be spatially well-resolved and that critical phenological stages can be identified in time.

To account for the effects of variable drought resilience and phenology, spatial resolutions finer than the GEO scale and temporal resolutions approaching daily time steps are required. TIR sensors on the polar-orbiting Landsat satellites, with a native resolution of 60–120 m, are the only current source of routine and global LST data that enable ET mapping at the sub-field scale. However, Landsat's revisit cycle of 16 days or longer, combined with gaps due to cloud cover, result in TIR data that are too temporally sparse to adequately capture ET variability at key phenological stages throughout the growing season (Kalma et al., 2008; Anderson et al., 2012). To address this limitation, an integrated multi-sensor approach was proposed by Anderson et al. (2011) to estimate ET at both high spatial and temporal resolution. This ET data fusion approach combines the benefits of the high spatial resolution (30 m, with thermal sharpening) of Landsat TIR images with the high temporal resolution (daily) of spatially coarser resolution polar-orbiting and geostationary satellites to provide daily field-scale ET estimates.

In this study, we extend the application of ESI-based stress detection and yield estimation down to field scales, to facilitate better separation of the diverse landcover types and variable phenologies characteristic of agricultural landscapes. We employ the ET fusion method to estimate daily ET, f_{RET}, and f_{RET} anomalies at the field scale over a corn/soybean production system located in the U.S. Corn Belt, including both rainfed and irrigated crops. The goal of this study is three-fold: first, to evaluate the accuracy of field-scale ET and f_{RET} retrievals in comparison with micrometeorological observations; second, to investigate the role of phenology in yield-f_{RET} correlations and explore optimal temporal alignment approaches; and lastly to demonstrate the utility of high-resolution ESI for yield estimation at field to county scales.

2. Methods

2.1. Multi-scale ET modeling scheme

The multi-scale ET mapping approach used here employs the Atmosphere – Land Exchange Inverse (ALEXI) surface energy balance model (Anderson et al., 1997, 2007a) and an associated flux disaggregation algorithm (DisALEXI; Norman et al., 2003; Anderson et al., 2004). ALEXI couples the Two-Source Energy Balance (TSEB; Norman et al., 1995; Kustas and Norman, 1999) model with a simple slab model of morning atmospheric boundary layer growth (McNaughton and Spriggs, 1986) to partition the surface energy budget between soil and canopy components of the composite scene:

$$Rn_s + Rn_c = (H_s + H_c) + (\lambda E_s + \lambda E_c) - G_0 \quad (1)$$

In Eq. (1) the subscripts "*s*" and "*c*" represent fluxes from the soil and canopy components, respectively; *Rn* is net radiation, λE is latent heat, *H* is sensible heat, and G_0 is the soil heat flux (all in units of $W\,m^{-2}$). Primary remote sensing inputs include LST, which constrains the sensible heat flux, and leaf area index (LAI), which governs the partitioning between soil and canopy fluxes. ET is in units of mass flux or $mm\,s^{-1}$ and can be computed from λE by dividing by the latent heat of vaporization required to evaporate 1 mm of water ($\lambda \sim 2.45 \times 10^6\, J\,m^{-2}$ at 20 °C).

For water-use management applications, daily values of ET (ETd, $mm\,d^{-1}$) are often more useful than instantaneous ET estimates. In this study, daytime-integrated ET estimates are extrapolated from the instantaneous latent heat fluxes retrieved from ALEXI using the ratio of instantaneous to daily insolation:

$$ETd = f_{SUN} * Rs_{24}/\lambda$$
$$f_{SUN} = \lambda E_{inst}/Rs_{inst} \quad (2)$$

where f_{SUN} is the ratio of instantaneous latent heat to instantaneous

insolation at the satellite overpass time, and Rs_{24} is the time-integrated daily insolation rate. While the evaporative fraction $\lambda E/(Rn\text{-}G_0)$ is often used to accomplish upscaling to daily total ET, recent studies have demonstrated that f_{SUN} provides comparable results and is less susceptible to retrieval errors associated with Rn and G_0 (Van Niel et al., 2011, 2012; Cammalleri et al., 2013, 2014).

The primary remote sensing inputs to ALEXI are time-differential measurements of the morning LST rise, typically obtained from TIR sensors on GEO platforms, and estimates of vegetation cover fraction which governs soil/canopy partitioning. The GEO time-differencing approach makes ALEXI more robust to errors in absolute LST retrieval, but limits application to the coarse spatial resolution of geostationary satellite data (3–10 km). To support higher spatial resolution mapping, an ALEXI disaggregation scheme (DisALEXI) was developed. DisALEXI uses TSEB, applied to higher resolution TIR and vegetation cover information obtained from polar orbiting or airborne platforms, to spatially downscale ALEXI daily flux fields (Anderson et al., 2012). Typical TIR data sources used in the disaggregation are Landsat (30-m resolution, employing a TIR sharpening technique/16-day revisit) and the Moderate Resolution Imaging Spectroradiometer (MODIS; 1 km/~daily).

2.2. ET data fusion

In this study, ET time series developed using Landsat and MODIS data are fused to create a multi-year "datacube" of Landsat-like (30-m resolution) images at daily time steps using the Spatial and Temporal Adaptive Reflectance Fusion Model (STARFM; Gao et al., 2006). STARFM compares a pair of Landsat and MODIS images collected on the same day and develops a spatially distributed weighting function that can be used to disaggregate MODIS images to the Landsat scale on neighboring days when clear Landsat data are not available (Gao et al., 2006). [For more details regarding the ET data fusion process, the reader is referred to Cammalleri et al., 2014, 2013; Semmens et al., 2015; Sun et al., 2017; Yang et al., 2017a, 2017b, with recent improvements in STARFM computational efficiency described by Gao et al., 2015.]

2.3. ALEXI Evaporative Stress Index (ESI)

The Evaporative Stress Index (Anderson et al., 2007b, 2011, 2013) describes temporal anomalies in the relative ET fraction:

$$f_{RET} = ET/ET_{ref} \tag{3}$$

where the numerator is the actual ET retrieved by satellite and ET_{ref} is the Penman-Monteith (FAO-56 PM) reference ET for grass as described by Allen et al., 1998, which is calculated using meteorological data described in Section 3.3.4. Normalization by reference ET is performed in order to reduce the impact of certain drivers of ET, such as insolation and vapor pressure deficit, which are less directly related to soil moisture limitations. In this study, daily f_{RET} is retrieved at the ALEXI/GEO scale (4 km) and at the Landsat scale (30 m) using the ET fusion model.

Year-to-year variability in the f_{RET} time series is then used to compute an anomaly index. To reduce day-to-day noise, the time series is first averaged over compositing windows of varying length (2, 4, 8 and/or 12 weeks), advancing at 7-day intervals and excluding days with cloud or snow cover. Next, at every pixel and 7-day interval, an anomaly metric is computed with respect to long-term normal f_{RET} conditions established for that pixel and interval using the full record archive.

For relatively long f_{RET} time-series (e.g. 10 years or longer), a standardized anomaly can be computed as:

$$v(d,y_k,i,j)' = \frac{\langle v(d,y_k,i,j)\rangle - \frac{1}{n}\sum_{k=1}^{k=n}\langle v(d,y_k,i,j)\rangle}{\sigma(d,i,j)} \tag{4}$$

where $\langle v(d,y,i,j)\rangle$ is the f_{RET} composite for day d, year y, and i, j grid location, $v(d,y,i,j)$ is the value on day d, n is the number of years in the period of record, and $\sigma(d,i,j)$ is the standard deviation in v for that compositing interval. This transforms the f_{RET} composite into a "z-score", normalized to a mean of zero and a standard deviation of one. Eq. (4) is used to generate real-time ESI maps covering North America for NOAA's GOES ET and Drought (GET-D) product suite (http://www.ospo.noaa.gov/Products/land/getd). At the GEO pixel scale, ESI values typically represent a mixture of signals from multiple sub-pixel land cover patches, each with potentially different phenological time behaviors.

For shorter f_{RET} time series, where σ can become noisy due to small sample size, we have found that a non-standardized anomaly in many cases provides more easily interpreted spatial patterns. In this initial 5-year study, a f_{RET} anomaly metric (referred to as Δf_{RET}) is computed as defined in Eq. (5):

$$\Delta v(d,y_k,i,j) = \langle v(d,y_k,i,j)\rangle - \frac{1}{n}\sum_{k=1}^{k=n}\langle v(d,y_k,i,j)\rangle \tag{5}$$

For operational applications, fused f_{RET} time series can be readily extended back to the beginning of the MODIS era, around 2001.

2.4. Crop-specific, phenology-corrected stress index

In this study, Eq. (5) is applied to 5-year f_{RET} time series developed at 30-m resolution using ET data fusion. A pixel-level assessment of f_{RET} anomalies at this scale over agricultural landscapes, however, may be dominated by differences due to rotating crops (e.g., corn to soybeans and vice versa) and year-to-year phenological variability and thus may not accurately reflect field-scale stress conditions. To address this issue, we take a crop-specific aggregation approach to stress index computation when using the 30-m ET datasets. For each year in the period of record, pixels associated with a given crop, c, are identified within a unit, u, of spatial aggregation (e.g., county scale), masking out all other land cover types. Furthermore, we introduce a more generic definition of the day-of-year index, d_p, which may include a potential temporal shift in alignment of f_{RET} curves from year-to-year to accommodate variability in phenology. Eq. (5) is reformulated as

$$\Delta v(d_p,y_k,c,u) = \langle v(d_p,y_k,c,u)\rangle - \frac{1}{n}\sum_{k=1}^{k=n}\langle v(d_p,y_k,c,u)\rangle \tag{6}$$

We apply Eq. (6) to maize crops at two scales: at the field scale over a collection of fields comprised of three AmeriFlux sites near Mead, NE; and at the county scale, using a crop classification mask to isolate specific crops. We evaluate three definitions of d_p: calendar date, days from emergence, and days from planting, to assess which temporal alignment provides the best predictors of crop yield.

3. Data and analyses

3.1. Study area

The study was conducted over the period 2010–2014 in an area near Mead, NE, located in the western part of the Corn Belt agricultural production region in the U.S. midwest (Fig. 1). The Mead experiment site hosts three long-term AmeriFlux flux tower installations, located within the University of Nebraska Agricultural Research and Development Center (Suyker et al., 2004). Fields Ne1 (48.7 ha) and Ne2 (52.4 ha) are irrigated (center-pivot), whereas field Ne3 (65.4 ha) is rainfed (Fig. 1). The Mead site was selected for this study of field-scale ET-yield relations because: 1) it includes multiple long-term flux towers in close proximity representing different crops and water management

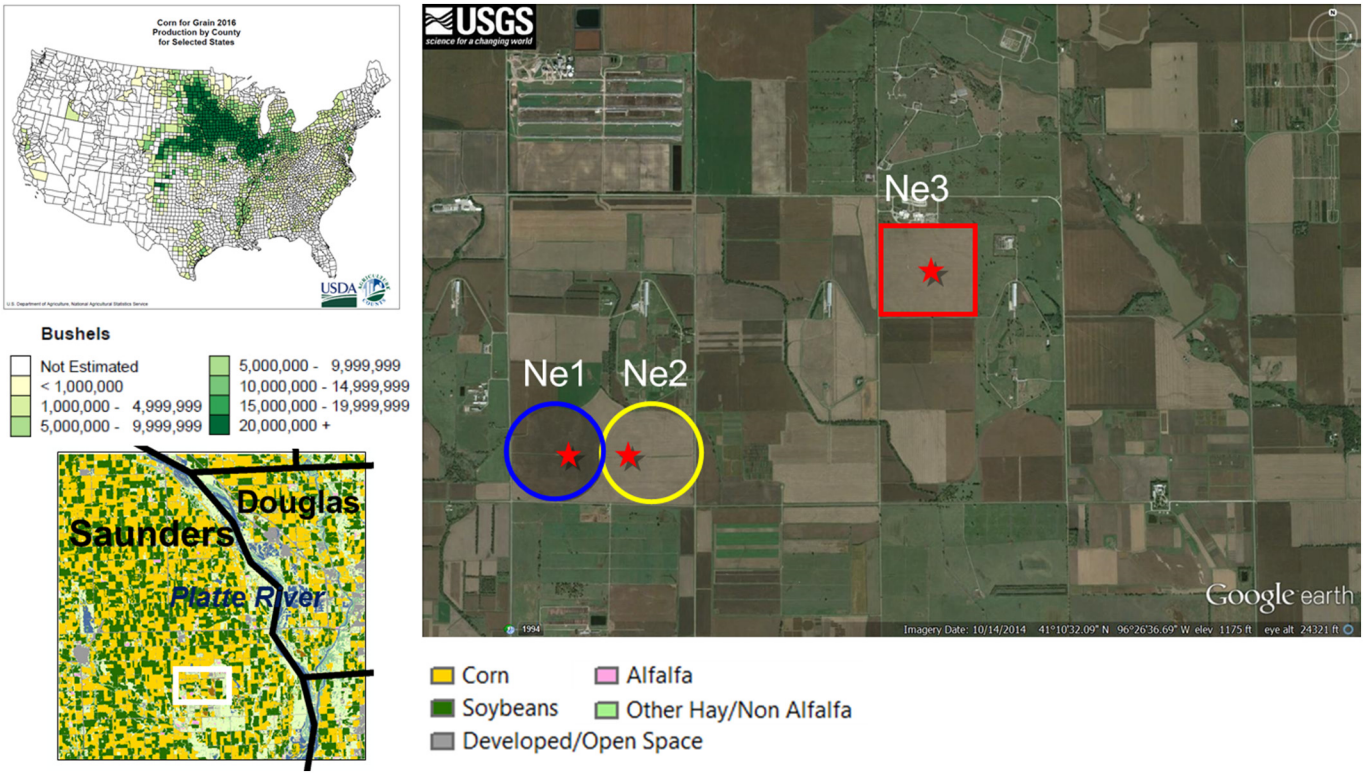

Fig. 1. Location of the study sites around Mead, NE, located within the U.S. Corn Belt (upper left panel, adapted from USDA Corn for Grain 2016 Production by County for Selected States). Field-scale analyses use flux and biophysical measurements from three AmeriFlux installations located within the University of Nebraska Agricultural Research and Development Center (right panel). County-scale analyses are conducted over portions of Saunders and Douglas Counties covered by the modeling domain, as outlined on a crop classification for 2012 extracted from the NASS Cropland Data Layer (CDL) product (lower left panel).

strategies under similar climate conditions; 2) multi-year yield, crop management and other biophysical data are available for the three flux site fields; and 3) the surrounding landscape is a mosaic of rainfed and irrigated crops, which will have variable response to drought and will pose a challenge to ET estimates based on water balance.

The Mead site is characterized by a humid continental climate, with an annual average temperature of 10.5 °C and an annual precipitation total of 780–790 mm. The topography of the area is essentially flat, with elevations around 350 m above sea level. This part of the Corn Belt is located within a high precipitation gradient band that exists around 100° W longitude, making this region particularly susceptible to periodic drought. Fig. 2 shows the drought status covering Nebraska and surrounding midwestern states over the study period, 2010–2014, as depicted by the U.S. Drought Monitor (USDM; Svoboda et al., 2002) and the 4-km, 4-wk composite ESI product. For most of this period, the USDM classified the Mead area as no drought or D0 (abnormally dry) during the peak growing season, with the exception of 2012 when D3-D4 (extreme to exception) drought conditions prevailed. Starting in May of that year, a "flash" drought enveloped much of the Corn Belt, driven by somewhat lower than normal precipitation but exacerbated by hot, dry and windy atmospheric conditions that quickly depleted available soil moisture. Otkin et al. (2016) demonstrated that the ESI showed early indications of the rapidly developing stress in this region, several weeks before it was reported in the USDM. Flash drought can often cause great losses for the agricultural sector, leaving the grower little response time to take adaptive measures (Otkin et al., 2015).

The Mead study area is comprised primarily of corn-soybean rotation cropping systems characteristic of the U.S. Corn Belt (Fig. 1). Crop planting, emergence, and harvesting dates during the study period are listed in Table 1 for the three flux tower fields. While these dates will vary from year to year and field to field based on climate and grower decisions, the Mead flux fields were managed similarly to fields in the surrounding area.

3.2. Micrometeorological and biophysical field measurements

The three fields highlighted in Fig. 1 are equipped with eddy covariance systems to collect measurements of latent heat (λE), sensible heat (H), CO_2, and momentum fluxes. The tower-based sensor packages include an omni-directional three-dimensional (3D) sonic anemometer (R2, Gill Instruments Ltd., Lymington, UK), a closed-path infrared CO_2/H_2O gas analyzer (LI6262, Li-Cor Inc., Lincoln, NE), and open-path infrared CO_2/H_2O gas analyzer (Model LI7500, Li-Cor Inc., Lincoln, NE). The eddy covariance sensors were mounted 3 m above ground level when the canopy was shorter than 1 m, and in maize were moved to 6 m later in the season to remain above the roughness sublayer. [For details regarding the flux and supporting micrometeorological instrumentations at Mead, readers are referred to Suyker and Verma, 2009.]

At the time of writing, flux data from these tower sites were available through 2013. Soil heat flux observations were corrected for heat storage in the soil layer above the plate. In addition, the energy balance closure (Rn-[$H + \lambda E + G_0$]) was assessed, yielding an average imbalance at the daily timescale of 16% of net radiation for all three sites combined over the flux period of record (2010–2013). In comparisons with modeled fluxes, latent heat and ET measurements are reported as observed (unclosed) and with a closure correction (closed) determined by partitioning the residual between the latent and sensible heat fluxes based on the observed Bowen ratio (Barr et al., 1994; Blanken et al., 1997; Twine et al., 2000).

In addition to micrometeorological data, episodic phenological dates such as planting, emergence, and harvesting were recorded at the three Mead AmeriFlux sites. Also, field-level yield data were collected for the 2010–2014 harvests in the Ne1, Ne2, and Ne3 fields. At larger

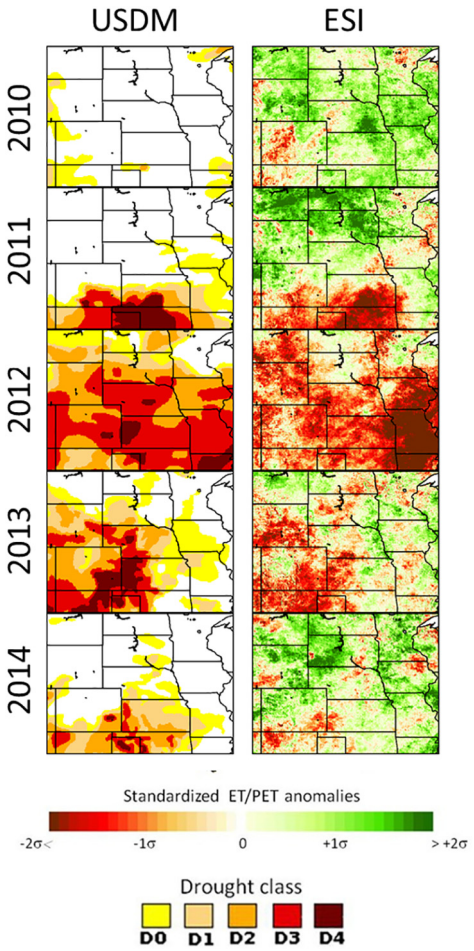

Fig. 2. ALEXI ESI (4-week composites; right column) and USDM (left column) for 2010–2014, both sampled near the end of July.

scales, yield and phenological data from various statistical reporting regions are available from reports published by the USDA National Agricultural Statistics Service (NASS). Yield survey data for Saunders and Douglas Counties, covering the major part of the study domain, were obtained from NASS Quick Stats. NASS crop progress reports (NASS CPR, 2017) for the state of Nebraska provide average planting and emergence dates characteristic of the state as a whole. These data were used in yield analyses conducted at the county scale.

3.3. ET model inputs

3.3.1. Geostationary satellite data

ALEXI was implemented at 4-km resolution over the continental United States (CONUS) using data from the Geostationary Operational Environmental Satellites (GOES). In combination, GOES-EAST (at 75°W) and GOES-WEST (at 105°W) provide brightness temperature observations over the full CONUS domain (Anderson et al., 2007a, 2007b).

3.3.2. MODIS data

Near-daily ET estimates at 1-km resolution were generated with DisALEXI by disaggregating the 4-km ALEXI ET fields using data from several MODIS standard products. Daily LAI maps were interpolated from the 4-day MODIS composite product (MCD15A3, Collection 5; Myneni, 2014) following the algorithm described by Gao et al. (2012a). LST and view angle maps were obtained from the Terra instantaneous swath 1-km product (MOD11_L2, Collection 5; Wan, 2014) and geolocation fields (MOD03). Land-surface albedo was extracted from the MODIS BRDF/Albedo CMG Gap-Filled Snow-Free Product (MCD43GF Collection 5; Schaaf et al., 2011).

To fill gaps in daily coverage due to clouds and swath limitations, a simple gap-filling and smoothing technique was applied to the MODIS ET retrievals. The ratio of ETd from MODIS DisALEXI and ALEXI was computed for each clear MODIS pixel. This ET ratio was then filtered, smoothed and gap-filled in time at each pixel using a Savitzky-Golay filter and spline interpolation technique. Gap-filled daily MODIS ET is recovered by multiplying this ratio by daily ALEXI ET.

3.3.3. Landsat data

Landsat 5, 7, and 8 data from 2010 to 2014 were acquired over the study area (path 28/row 31). Excluding scenes with snow cover and/or > 30% cloud cover, a total of 138 scenes of Landsat multiband and surface reflectance images were processed, with an average frequency of two weeks between images and a maximum gap of 32 days (Table 2). Landsat LST was derived from thermal band observations by atmospherically correcting at-sensor brightness temperature via MODTRAN (Berk et al., 1989) following procedures documented by Cook et al. (2014). The resulting LST maps at native spatial resolution of 120 m (Landsat 5), 60 m (Landsat 7) or 100 m (Landsat 8) were sharpened to the 30-m resolution of the Landsat reflectance bands using a Data Mining Sharpener (DMS) technique (Gao et al., 2012a). Shortwave reflectance band data were calibrated and atmospherically corrected using the Landsat Ecosystem Disturbance Adaptive Processing System (LEDAPS; Masek et al., 2006). Leaf area index at 30-m resolution on Landsat overpass dates was derived using a regression tree approach trained by MODIS 1-km LAI sample data (Gao et al., 2012b).

Table 1
Phenological dates (day of year, DOY) associated with crops grown at the three flux tower sites near Mead, NE (Courtesy of Dr. Andy Suyker).

	Year	Crop	Planting DOY	Emergence DOY	Harvesting DOY
Ne1	2010	Maize	109	124	264
41°09′54.2″N	2011	Maize	138	146	299
96°28′35.9″W	2012	Maize	115	123	284
	2013	Maize	119	134	295
	2014	Maize	111	127	301
Ne2	2010	Maize	111	133	260
41°09′53.5″N	2011	Maize	139	147	300
96°28′12.3″W	2012	Maize	116	124	303
	2013	Maize	121	136	296
	2014	Soybean	141	147	284
Ne3	2010	Soybean	140	148	280
41°10′46.8″N	2011	Maize	123	134	292
96°26′22.7″W	2012	Soybean	136	142	275
	2013	Maize	134	142	295
	2014	Soybean	140	147	282

Table 2
List of Landsat 5,7, and 8 scenes (path 28/row 31) used in this study (2010–2014).

	2010	2011	2012	2013	2014
	L5 L7	L5 L7	L7	L7 L8	L7 L8
Jan					2
Feb				2	1
Mar	1		1		1
Apr	1	1	2	2	2
May	2	2	1		1
Jun		2	2	1	2
Jul	1	2	2	1	2
Aug	2	4	1	1	1
Sep	2	2	1	1	2
Oct	2	2	2	3	2
Nov	2	1		1	
Dec					

Note: L5: Landsat 5, L7: Landsat 7, L8: Landsat 8. In 2012, only L7 was functional. L8 was launched in 2013.

3.3.4. Regional meteorological inputs

Regional meteorological inputs to ALEXI and DisALEXI, including solar radiation, wind speed, air temperature, and vapor pressure, were obtained from the Climate Forecast System Reanalysis (CFSR; Saha et al., 2014). The meteorological datasets were resampled from their native resolution of 0.25° onto the ET modeling grids (4 km, 1 km and 30 m), and then spatially smoothed to remove coarse-scale artifacts in the resulting ET retrievals. These data were also used to compute reference ET time series for the f_{RET} datasets.

3.3.5. Land cover

Land cover classification data are used to specify surface roughness parameters within ALEXI/DisALEXI. The 1-km resolution global land cover dataset from the University of Maryland (Hansen et al., 2000) is used in the operational ALEXI modeling framework. For the DisALEXI model, consistency between the MODIS and Landsat-derived ETd is critical to ensure fusibility. Consequently, the 30-m National Land Cover Dataset (NLCD; Homer et al., 2015) was used at its native resolution for the Landsat disaggregation, and aggregated to 1-km resolution by majority class assignment for the MODIS disaggregation. While not used as input to the ET modeling, the NASS Cropland Data Layer (CDL; Boryan et al., 2011) – developed annually at 30-m spatial resolution – was used to separate corn and soybean pixels within the modeling domain for yield analyses.

3.4. Analyses

3.4.1. Crop-specific stress index at 30-m resolution

Using Eq. (6), crop-specific f_{RET} anomalies (Δf_{RET}) were computed from the 30-m f_{RET} time series over the period 2010–2014. Unlike standard ESI computations for 4-km pixels, the normal (mean) conditions cannot be reasonably computed per-pixel at the 30-m scale in this kind of landscape due to the rotation of crops from year-to-year in a given field. Rather, we average f_{RET} over pixels associated with a specific crop within a given aggregation unit prior to establishing the normal annual curve. This “regional” crop-specific normal curve is then used along with crop-masked f_{RET} to compute Δf_{RET} at the field or 30-m pixel scale. The value added by the improvement in spatial resolution in ESI from 4-km to 30-m, enabling crop specificity and phenological alignment of annual f_{RET} time series, was assessed in terms of improved correlation between Δf_{RET} and yield observations at field and county scales.

The first tests were conducted on the fields sampled by the three flux towers: Ne1, Ne2, and Ne3. Because soybeans were represented in only 4 of the 15 crops planted in these three fields during the 5-year study period (Table 1), our analysis focuses on corn production. Annual time series of field-averaged f_{RET} were computed for each of the corn-site years (11 total). The normal (mean) condition, defined in the second term in the right part of Eq. (6), was computed by averaging all time series for all corn-planted AmeriFlux fields over the five years. To correct for the impact of phenology on the f_{RET} anomalies, we tested three temporal alignments: based on calendar date, days from planting, and days from emergence. In this case, emergence and planting dates recorded in-field were used (Table 1).

We applied a similar crop-specific, phenology-corrected f_{RET} anomaly analysis over the full domain at 30-m resolution, using phenological data from the NASS CPR. In this test, the normal f_{RET} curve for corn developed at the flux fields was used, as described above. Anomalies in f_{RET} were then computed per-pixel with respect to this normal curve. An emergence-date phenological correction was also evaluated at the county scale, assuming each corn field in a given year emerged at roughly the same date as identified in the NASS CPR.

In an operational mode, for large-area ESI mapping, normal curves would be developed at a relevant administrative scale (e.g., county or district) rather than from a few test fields.

3.4.2. Yield - Δf_{RET} correlations

Yield - Δf_{RET} correlations for AmeriFlux corn fields were quantified using the Pearson correlation coefficient as a function of f_{RET} composite date (d_p). The peak in this correlation curve identifies the date when Δf_{RET} has maximum predictive power for yield estimation. Improvements in performance due to pixel scale or phenological correction were assessed in terms of impacts on peak correlation.

Yield - Δf_{RET} regression functions, developed at field scale for the date of peak correlation, were also applied to the gridded Δf_{RET} data to generate yield estimates at 30-m over the full study domain. First, a Δf_{RET} map was generated for each year, extracting values from the date of peak correlation. Then the field-scale yield - Δf_{RET} function for that date was applied to all corn pixels in each year.

The resulting 30-m yield maps were compared to county-level yield estimates from NASS. The study domain covers part of two both Saunders and Douglas Counties (Fig. 1). The NASS crop data layer (NASS CDL, 2017) suggests that landcover in the Mead study area is similar to the agricultural landscape in the remaining parts of the two counties. Therefore, we assume that Δf_{RET} and yields in the sub-regions intersected by our domain will be representative of the corn fields in these two counties (subject to differences in irrigation usage). Pixel-level modeled yield estimates were averaged over each county (Saunders and Douglas) and compared to the NASS estimates. Again, this was tested for calendar, planting and emergence date temporal alignments.

4. Results

4.1. Model evaluation on Landsat overpass dates

Flux disaggregation to Landsat resolution allows a direct evaluation of model output with tower-based eddy covariance observations, which sample a surface footprint with dimension on the order of 100 m depending on tower height and stability conditions. Fig. 3 compares modeled and measured daytime-integrated surface energy fluxes (net radiation, latent heat, sensible heat, soil flux, and solar radiation) on Landsat overpass dates at the three flux sites. In general, modeled fluxes vs. in-field measurements fall along the one-to-one line, indicating a good partitioning among the main energy budget components. Quantitative measures of all flux comparisons further corroborate the good model performance (Table 3). Several metrics including MBE (mean bias error), MAE (mean absolute error), RMSE (root mean square error), and % error (percent error, defined as the ratio of MAE and the mean observed flux) were selected to quantify the model performance as suggested by Willmott (1982) and Willmott and Matsuura (2005).

Insolation (Rs) and net radiation (Rn), which are the major energy

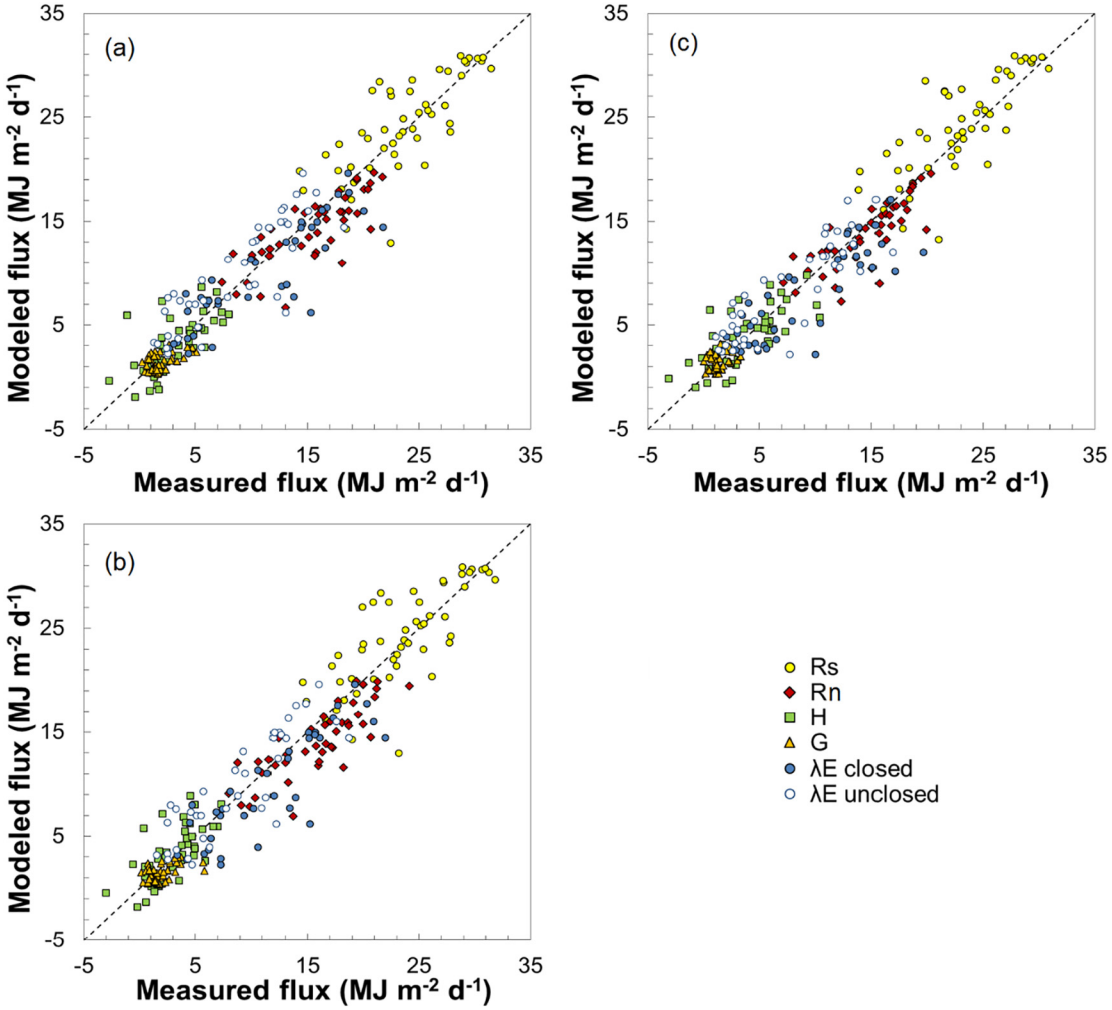

Fig. 3. Comparisons of observed and Landsat-retrieved daytime integrated fluxes on Landsat overpass dates at Ne1 (a), Ne2 (b), and Ne3 (c). Rs: solar radiation; Rn: net radiation; H: sensible heat; G: soil heat flux; λE: latent heat flux, where closed indicates energy balance closure using Bowen Ratio technique (Twine et al., 2000), while unclosed indicates that energy balance closure was not imposed on the measurements.

source for ET, agree well with local measurements. Mean bias errors for both sensible heat and soil heat fluxes are low, and the RMSE is comparable to that for the other flux components. The larger percent errors for these fluxes are due to the lower magnitude of the mean observed *H* and *G*. Modeled latent heat fluxes are compared to observations both with and without closure correction. Notably better agreement is obtained with the closed results, likely reflecting both the closure constraints imposed within the model framework as well as measurement errors. Model performance is similar between the three AmeriFlux sites. For all three sites combined, the MAE in λ*E* is 2.15 MJ m^{-2} d^{-1} for Landsat dates, or about 20% of the mean observed flux. This is consistent with typical errors obtained in previous flux measurement intercomparison studies (Kustas and Norman, 1997; Kalma et al., 2008) and with typical closure errors in eddy covariance datasets (Wilson, 2002).

4.2. Evaluation of fused daily ET time series at the flux sites

Time series of observed and modeled daily ET from the fused time series 2010 to 2013 are shown in Fig. 4 for all three flux sites. The top axis shows the amount of water received on the land surface. Note that for irrigated sites Ne1 and Ne2, the amount of water received includes both rainfall and irrigation applications.

The fusion model reproduces the observed seasonal and interannual ET trends well at both the irrigated and rainfed sites. Statistical metrics of model-measurement agreement at daily, monthly, and nominal growing season (DOY 100–300) timescales are provided in Table 4. Compared with closed observations, RMSE is 1.2 mm d^{-1} and MAE is 1.0 mm d^{-1} for ET retrievals on daily time steps, for all three sites combined. These daily accuracies are close to the average obtained from prior ET fusion experiments using this modeling system (Cammalleri et al., 2013, 2014; Semmens et al., 2015; Sun et al., 2017; Yang et al., 2017a, 2017b). Because these time series include both direct and interpolated retrievals, and span multiple years, crops and water management strategies, comparisons with ET model accuracies reported in the literature – which may reflect a different diversity in conditions – are not straight forward. However, Seguin et al. (1999) cite 1.5 mm d^{-1} as an average model accuracy, and suggest 0.8 mm d^{-1} as a target for agricultural management at field scale. At the monthly time step, percent error in the fused ET time series is reduced to 12–17% due to averaging of random errors. After aggregating the daily ET to seasonal water use, percent errors are 4–9% for the three fields.

To demonstrate the differential response of irrigated and rainfed crops to drought in greater detail, annual ET time series from 2010 and 2012 are compared in Fig. 5. Rainfall in 2010 was similar to the long-term average value, but 2012 can be classified as a “drought year” with precipitation half that of 2010. Rainfall deficits associated with the 2012 drought are evident at the rainfed Ne3 site, with little precipitation occurring from July to August. The regular spikes in precipitation at Ne1 and Ne2 during this timeframe are due to irrigation events. In

Table 3
Summary of the statistical indices quantifying model performance for daytime-integrated surface energy fluxes on Landsat overpass dates at the three fluxes stations (unit: MJ m^{-2} d^{-1}).

		Rs	Rn	H	G	λE (closed)	λE (unclosed)
Ne1	Mean O	23.49	15.38	3.12	1.90	10.89	8.56
	Mean P	24.20	14.22	3.21	1.43	9.97	9.97
	RMSE	3.15	2.65	2.03	1.11	2.82	3.01
	MBE	0.71	−1.16	0.09	−0.47	−0.92	1.41
	MAE	2.29	2.06	1.54	0.95	1.85	2.58
	%error	9.76	13.42	49.45	49.81	16.95	30.12
Ne2	Mean O	23.55	15.98	3.01	1.97	11.63	8.77
	Mean P	24.19	14.20	3.38	1.51	9.78	9.78
	RMSE	3.27	2.83	2.56	1.18	3.27	2.82
	MBE	0.64	−1.79	0.37	−0.47	−1.85	1.01
	MAE	2.35	2.24	1.63	0.88	2.32	2.42
	%error	9.98	13.99	54.29	44.85	19.98	27.53
Ne3	Mean O	22.92	14.48	3.90	1.34	9.57	7.50
	Mean P	24.19	13.64	4.02	1.61	8.29	8.29
	RMSE	3.21	2.28	2.21	0.95	2.97	2.59
	MBE	1.28	−0.83	0.12	0.27	−1.28	0.79
	MAE	2.41	1.65	1.77	0.81	2.29	2.16
	%error	10.53	11.38	45.37	60.00	23.91	28.72
Three sites combined	Mean O	23.32	15.28	3.38	1.74	10.67	8.27
	Mean P	24.19	14.02	3.50	1.52	9.41	9.41
	RMSE	3.21	2.60	2.11	1.09	3.02	2.81
	MBE	0.87	−1.26	0.12	−0.23	−1.26	1.14
	MAE	2.35	1.99	1.65	0.88	2.15	2.38
	%error	10.09	12.99	48.79	50.50	20.13	28.82

Mean O: the mean value of observed flux; Mean P: the mean value of predicted flux; RMSE: root mean square error; MBE: mean bias error; MAE: mean absolute error; R_s: solar radiation; Rn: net radiation; G: soil heat flux; H: sensible heat flux; λE: latent heat flux. The closed values indicate comparisons with flux observations closed using the Bowen ratio technique (Twine et al., 2000), while unclosed indicates that energy balance closure was not imposed on the measurements.

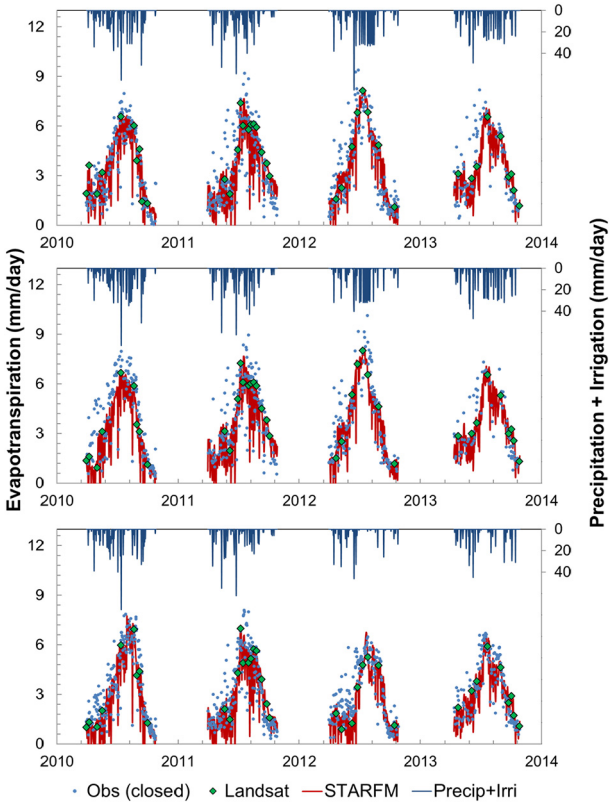

Fig. 4. Time series of closed ET observations (blue dots), 30-m ET retrievals on Landsat overpass dates (green diamonds), and daily ET estimates from STARFM (red line) at Ne1 (top), Ne2 (middle), and Ne3 (bottom) for 2010–2013. Rainfall and irrigation events are shown on the top of each panel as blue bars. Note that Ne1 and Ne2 are irrigated fields while Ne3 is rainfed. (For interpretation of the references to colour in this figure legend, the reader is referred to the web version of this article.)

both irrigated sites, ET is higher during the drought year than in the normal year. This likely reflects both surplus irrigation in response to the drought, and the higher evaporative demand in that year. As indicated by Carr et al. (2016) based on farmers' reports, irrigation in eastern NE increased dramatically in 2012 in comparison with adjacent years. In the rainfed site (Ne3), in the absence of supplemental irrigation, ET is lower during the drought year as would be expected.

In terms of seasonal water use, the model estimates agree well with the closed ET observations for most years, collectively underestimating the mean observed seasonal value of 680 mm by only 4% (Fig. 6). Among the four years, water use in 2012 is unique, with seasonal ET increasing at the irrigated Ne1 and Ne2 sites, and decreasing at rainfed Ne3 site in response to the Midwest drought in that year (right panel).

4.3. Spatial patterns in ET

Fig. 7 shows the seasonal cumulative ET over an area (35 km × 35 km) around the Mead site, demonstrating variability in spatial water use patterns for the period 2010–2013. Some general features emerge in the comparison. The riparian zones along the Platte and Elkhorn Rivers maintain high ET even in the drought year due to continuous surface and subsurface moisture supply. In other parts of the domain, ET is highest in 2010 – the year with the highest rainfall within the 2010–2013 timeframe but considered “normal” with respect to long-term average rainfall rates. Center pivot-irrigated fields (circular features) are not easily identified in 2010 and 2011, but become particularly pronounced in the drought year of 2012 in contrast with the surrounding rainfed land surface. Evidence of irrigation persists into 2013, perhaps indicating a shift in water management strategy in response to the 2012 drought.

Temporal patterns of ET accumulation during the growing season between normal (2010) and drought (2012) years are contrasted in Fig. 8, which shows gridded ET time series over a 12 × 12 km box that includes the three flux tower sites near the center. These time series highlight contrasting trends in water use patterns that occurred over the landscape during these years, as indicated in Fig. 6. Two large rainfed

Table 4
Summary of the statistical indices quantifying model performance for ET on daily, monthly and seasonal water use over growing season at the three fluxes stations (unit: mm).

		NE1		NE2		NE3		Three sites combined	
		ET closed	ET unclosed	ET closed	ET unclosed	ET closed	ET unclosed	ET closed	ET unclosed
Daily	Mean P	3.50	3.50	3.44	3.44	2.86	2.86	3.27	3.27
	Mean O	3.41	2.84	3.72	2.86	2.96	2.48	3.36	2.72
	RMSE	1.27	1.36	1.09	1.04	1.07	1.07	1.25	1.24
	MBE	0.09	0.67	−0.27	0.58	−0.10	0.38	−0.09	0.55
	MAE	1.00	1.13	0.54	0.5	0.85	0.87	0.98	1.01
	%error	29.33	39.76	29.19	36.43	28.62	34.96	29.12	37.19
Monthly	Mean P	104.87	104.87	102.09	102.09	84.17	84.17	97.04	97.04
	Mean O	100.78	84.41	113.44	87.12	86.37	72.74	100.2	81.42
	RMSE	19.29	29.48	24.34	23.4	12.32	17.19	19.29	23.89
	MBE	4.08	20.46	−11.35	14.97	−2.20	11.43	−3.15	15.62
	MAE	14.86	24.52	18.78	19.21	10.36	14.31	14.67	19.89
	%error	14.74	29.05	16.55	22.05	12.00	19.68	14.64	23.76
Seasonal	Mean P	699.14	699.14	690.61	690.61	566.28	566.28	652.01	652.01
	Mean O	688.02	570.3	747.98	574.33	594.34	497.25	676.78	547.3
	RMSE	32.34	131.44	76.15	128.56	29.24	71.22	50.66	113.84
	MBE	11.12	128.84	−57.37	116.28	−28.06	69.03	−24.77	104.72
	MAE	28.33	128.84	57.37	116.28	28.06	69.03	37.92	104.72
	%error	4.12	22.59	7.67	20.25	4.72	13.88	5.60	19.13

Mean O: the mean value of observed flux; Mean P: the mean value of predicted flux; RMSE: root mean square error; MBE: mean bias error; MAE: mean absolute error; % error: mean absolute error divided by mean observed flux; ET: evapotranspiration. The closed indicates energy balance closure using Bowen ratio technique (Twine et al., 2000), while unclosed indicates that energy balance closure was not imposed on the measurements.

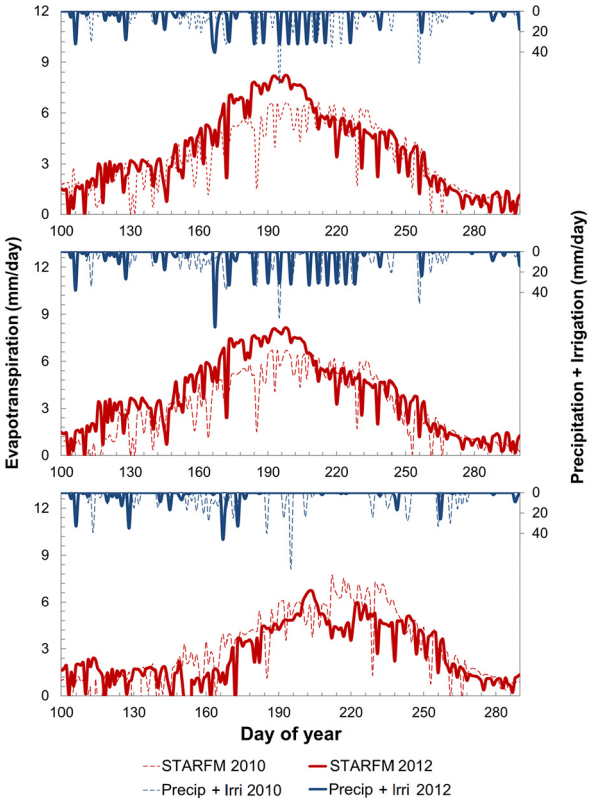

Fig. 5. Modeled ET total precipitation (rainfall + irrigation) over growing season in Ne1 (top), Ne2 (middle), and Ne3 (bottom). Solid lines represent 2010 (normal year); dashed lines represent 2012 (drought year).

experimental fields associated with the Mead research site dominate the local water use in 2010 (black boxes in Fig. 8). In contrast, these rainfed fields show low cumulative ET throughout the 2012 growing season, whereas impacts of center pivot irrigation become evident mid-year. While overall cumulative ET in 2012 is lower than 2010 in most of the fields, in these irrigated fields the cumulative ET in 2012 often exceeds that of 2010 due to higher atmospheric demand and irrigation in response to drought.

4.4. Yield - Δf_{RET} correlations at tower sites

Relationships between corn yield and f_{RET} anomalies at the three flux sites were investigated for the period 2010–2014 at both the ALEXI 4-km (Fig. 9, top row) and Landsat 30-m pixel scale (Fig. 9, rows 2–4) as obtained from the daily fused ET datacube. A 4-week moving window advancing at daily time steps through the growing season was applied to f_{RET} and f_{RET} anomalies in Fig. 9 to suppress day-to-day noise. A single ALEXI time series is plotted for each year, extracted from the 4-km pixel containing the 3 AmeriFlux sites. For Landsat, multiple points per year are available in some cases depending on how many AmeriFlux fields were planted in corn (irrigated and/or rainfed) in a given year.

The first two columns in Fig. 9 show the growing season f_{RET} and Δf_{RET} time series at the ALEXI and Landsat resolutions, as well as the impact of aligning these time series on calendar day vs. phenological dates (days from planting and days from emergence, as determined from ground-based observations). The ALEXI f_{RET} time series have lower amplitudes (varying between 0.4 and 0.9) due to averaging over multiple sub-pixel land cover types with varying phenology and moisture conditions. In contrast, the daily Landsat-scale f_{RET} for pure corn pixels varies between 0.2 and 1.25, the latter consistent with FAO peak crop coefficients for corn (Allen et al., 1998). By removing normal seasonal variability from f_{RET}, the anomaly Δf_{RET} (2nd column in Fig. 9) shows the water stress departure from normal (mean) conditions.

Alignment based on the phenological date tends to collapse the individual Landsat f_{RET} curves around the normal (climatological) curve and reduce anomalies in Δf_{RET}. This is consistent with the hypothesis that some component of the ALEXI ESI signal over the Corn Belt is induced by phenological shifts from year to year and therefore unrelated to moisture conditions. For example, 2011 had a relatively late planting and emergence date (Table 1). Alignment by calendar date gives a false dry signal during the first part of the season in the irrigated fields (Ne1 and Ne2). The 2012 anomaly curves at Landsat scale show the classic signals of a flash drought (Otkin et al., 2018). The intense heat wave and windy conditions that year led to high ET rates early in the season (positive Δf_{RET}), followed by a period of rapidly depleting available soil moisture and increasing stress (below normal f_{RET}).

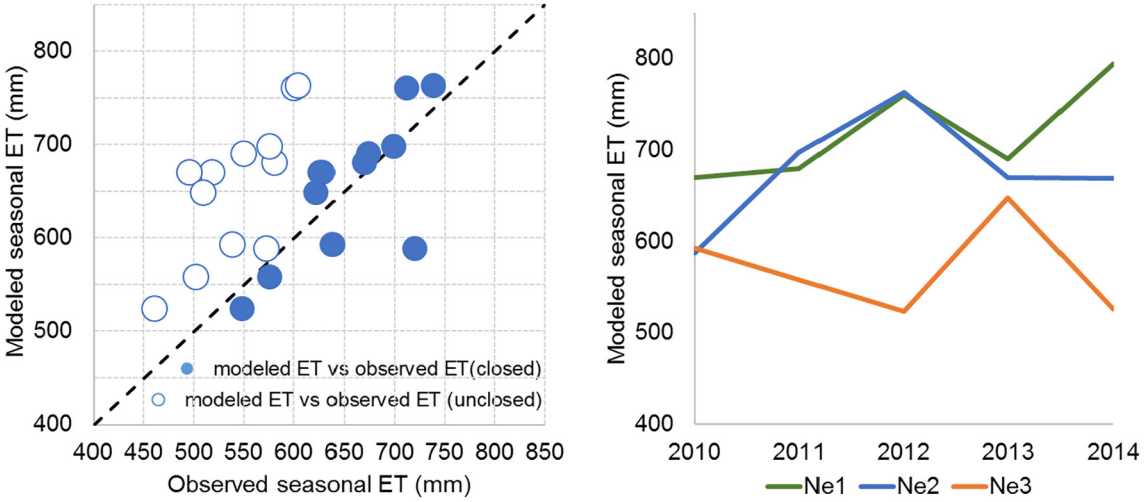

Fig. 6. Comparison of modeled and observed seasonal ET (left); modeled seasonal ET at Ne1, Ne2, N3, 2010–2014 (right). Seasonal ET is the computed as a cumulative value for DOY 100–300.

The third column in Fig. 9 shows the correlation coefficient (r) between annual field-scale yield measurements and Δf_{RET}, with a scatter plot of yield vs. f_{RET} extracted on the date of peak correlation shown in the final column. The 4-km ALEXI f_{RET} shows relatively weak correlations with yields (peak value of 0.3), with a negative relationship later in the season driven primarily by 2012. At the Landsat scale, however, where the individual fields can be isolated, the correlations become much stronger. Peak correlation improves from $r = 0.82$ using a calendar date alignment to $r = 0.88$ and $r = 0.94$ when f_{RET} curves are aligned on planting date and emergence date, with emergence date alignment yielding the highest correlation. At Landsat-scale, the peak correlation occurred 68 days after emergence, corresponding to the silking stage for maize (Hanway, 1966). Moisture stress occurring during silking is known to have a strong impact on corn yields (e.g., Denmead and Shaw, 1960). Therefore, f_{RET} time series datasets show potential for conveying temporally explicit water stress information to crop simulation models.

This experiment demonstrates that the spatial resolution of Landsat provides a useful scale for assessment of yield and water productivity within the U.S. Corn Belt, where 30-m pixels can typically differentiate between different crop types and phenological stages. In contrast, the ALEXI pixel scale includes signals with a mixture of subpixel crop types at different stages of development. The date of peak signal from the three temporal alignments tested converges around July. This is likely

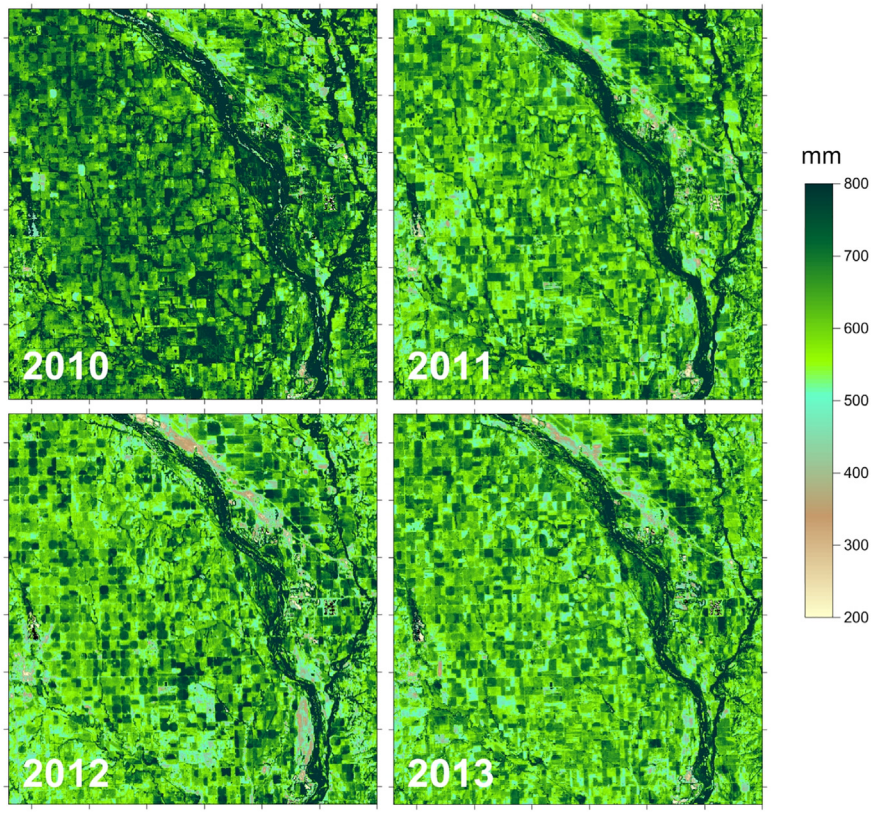

Fig. 7. Cumulative ET over growing season (DOY100–300) for 2010–2013 within the Mead domain.

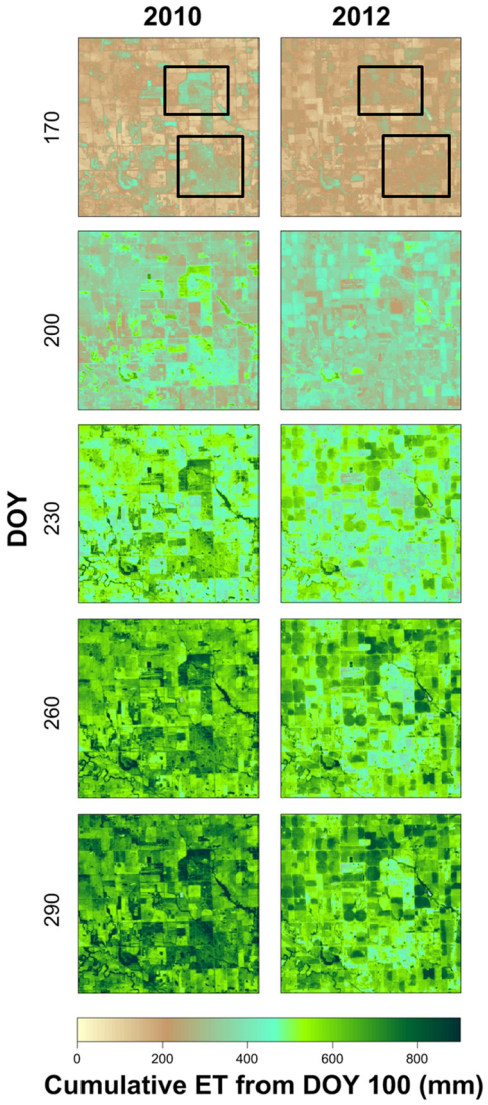

Fig. 8. Spatial time series (every 30 days) of cumulative ET in 2010 (left column) and 2012 (right column) over a 12 km × 12 km area including the three flux sites. Black boxes in top panel highlight large rainfed experimental fields that exhibit contrasting water use behavior in comparison with surrounding center-pivot irrigated fields.

specific to corn grown in this region. For more general applications, optimal dates for yield estimation using f_{RET} will need to be derived regionally for each target crop.

4.5. Yield estimation at county level

Using the regression functions derived at field scale on the peak correlation date evident in Fig. 9, we applied these functions to pixels classified in the CDL as corn to map corn yield over the full study domain. As in the field-scale analyses, three f_{RET} temporal alignments were tested: calendar date, planting date and emergence date. In this case, however, phenological dates were extracted from the NASS crop progress reports at the district level. Dates when the district achieved about 50% planting or 50% emergence were chosen to represent crop development in a regional context. Maps of estimated corn yield are shown in Fig. 10 for 2010–2014 assuming emergence date alignment (non-corn pixels are blanked in these maps).

County-averaged corn yield estimates from the optimal regression function were then compared to NASS yield data for Douglas and Saunders Counties, converted from Bu/acre to Mg/ha (1 Bu equivalent is 39.368 Mg). Note that only a portion of these counties is sampled within the ET fusion domain, and in the case of Douglas Co, a significant fraction of the sampled area includes forest and riparian land covers. Scatter plots of NASS and estimated yields (assuming calendar date and emergence date alignment) are shown in Fig. 11, with statistical metrics of comparison for all three alignments summarized in Table 5. These comparisons further corroborate the value of f_{RET} retrieval via data fusion in reducing errors in yield estimates. Even at ALEXI resolution (4 km), adjusting f_{RET} to emergence date alignment prior to anomaly computation improves correlations with yield estimates at the county level from 0.28 to 0.80. Disaggregation of ALEXI ET to Landsat scale further enables emergence date alignment at field scale and increases the correlation from moderate (0.47; calendar date) to high (0.93; emergence date) values. This is because at this scale, signals from non-corn fields, such as more drought-resilient forest and riparian patches, can be isolated and removed.

The yield maps in Fig. 10 and the cumulative water use estimates in Fig. 7 can be used to compute crop water productivity (i.e. yield per unit of water used) - a critical metric of sustainability in agricultural production systems. Combining yield from Fig. 10 with seasonal ET from Fig. 7 results in an average water productivity for corn of 1.5 kg/m^3 for the period 2010–2014. This value is similar to field estimates of 1.4 kg/m^3 computed from farm-scale yield and irrigation data collected in central Nebraska for the period 2005–2013 (Carr et al., 2016).

5. Discussion

5.1. Temporal upscaling via data fusion

Actionable information for agricultural water management at field scale requires data at both high spatial (< 100 m) and temporal (~daily) resolution – joint criteria that are not currently met by any single Earth observing satellite system with thermal imaging capabilities. Several methods have been proposed to upscale high-resolution ET retrievals on Landsat overpass dates to full seasonal coverage, including assumptions of temporally uniform f_{RET} between overpasses (Senay et al., 2013), or spline interpolation to daily values (Allen et al., 2007) with corrections to the soil evaporation component via soil water balance accounting that require additional rainfall and soil texture information (Kjaersgaard et al., 2011).

The fusion system described here attempts to diagnostically capture changes in surface moisture conditions that occur at the MODIS scale (1-km) between Landsat overpasses. While this has the potential to recover wetting signals due to larger precipitation events, it cannot reproduce rapid changes occurring at finer spatial scales, for example due to irrigation applications or harvests in individual fields. Data fusion therefore should not be considered a substitute for more frequent collection of actual Landsat imagery. In general, errors in fused ET time series tend to be larger for sites where cloud cover precludes at least one clear Landsat scene per month – particularly during the rapid spring green-up phase. The new Visible Infrared Radiometer Suite (VIIRS) on board the Joint Polar Satellite System (JPSS) platforms – the MODIS follow-on mission – provides near-daily TIR data in a 375-m single channel, which will benefit recovery of even smaller-scale daily changes in the fused ET datastream.

5.2. Improving ESI performance over agricultural landscapes

A major motivation for this study was to identify means for improving the performance of regional ESI products over intensively managed agricultural areas, such as in the core of the U.S. Corn Belt. Decreased correlations between ESI and USDM drought classes as well as other standard drought indicators observed over this region, particularly in southern Minnesota and northern Iowa (Figs. 6 and 7 in Anderson et al., 2011), are related to locally amplified noise in the ESI time series (Fig. 10 in Anderson et al., 2013). In these intensively

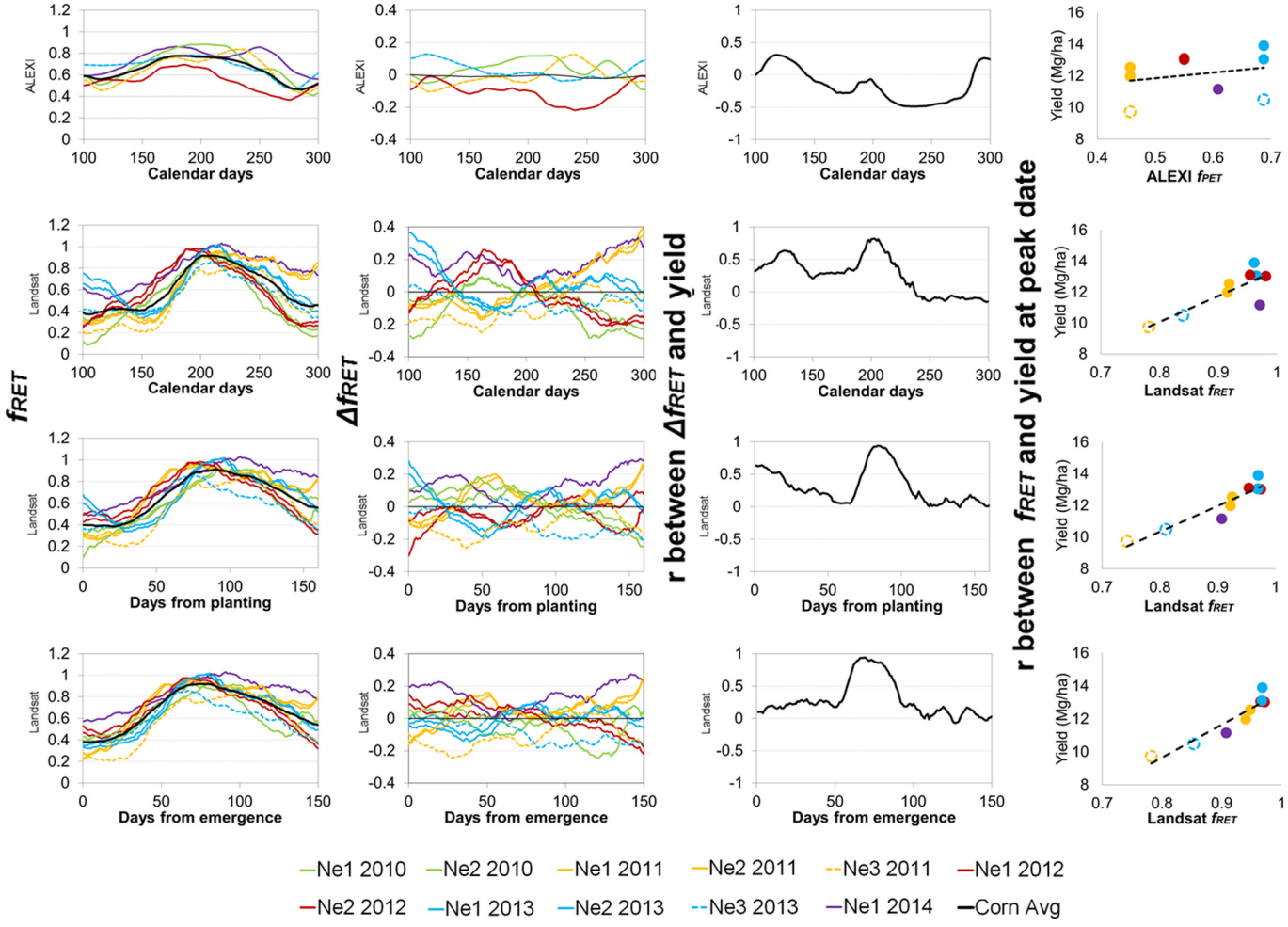

Fig. 9. Analysis of temporal relationship between f_{RET} and yield at the ALEXI pixel scale (top row) and Landsat pixel scale (rows 2–4) obtained for corn crops at the Mead AmeriFlux sites. First two columns show f_{RET} (Column 1) and f_{RET} anomaly (Column 2) plotted against calendar date (rows 1, 2) and phenological dates starting from planting (row 3), and emergence (row 4). Column 3 shows the correlation coefficient regressing f_{RET} anomalies and corn yields as a function of composite date. Column 4 shows scatter plots of yield vs. f_{RET} obtained on the date of peak correlation. A 4-week moving window advancing at daily time steps through the growing season was applied to f_{RET} and f_{RET} anomalies to suppress noise - the date on the x-axis corresponds to the center of the moving window.

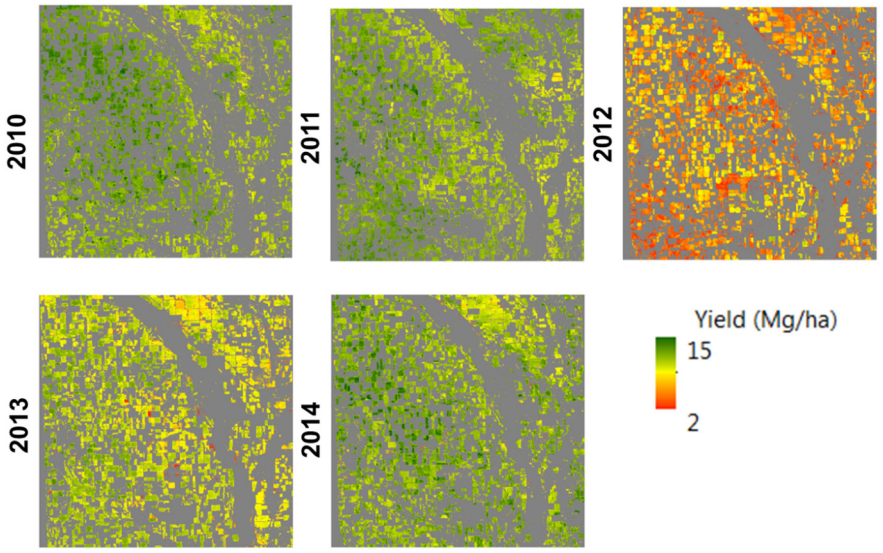

Fig. 10. Corn yield estimates for 2010–2014 using regression curves developed from field-scale datasets on date of peak correlation, using f_{RET} alignment based on emergence date. Gray indicates pixels not classified as corn according to the NASS CDL.

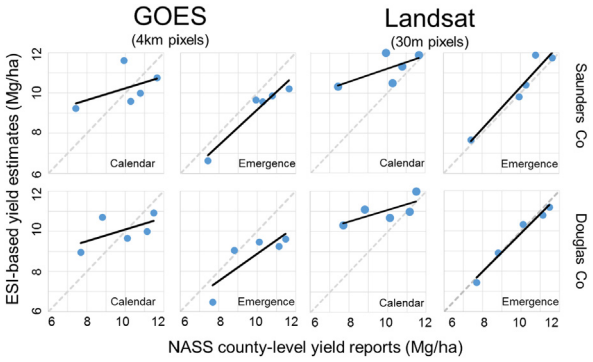

Fig. 11. Comparison of corn yields reported by NASS yield and yields estimated based on ESI at ALEXI and Landsat pixel scales for Saunders County and Douglas County for 2010–2014. Alignments based on calendar and emergence date are used.

Table 5
Statistical metrics comparing observed and predicted yields in Saunders and Douglas County 2010–2014.

Alignment		Calendar		Planting		Emergence	
Scale		ALEXI	Landsat	ALEXI	Landsat	ALEXI	Landsat
Saunders Co.	r^2	0.24	0.44	0.22	0.43	0.93	0.93
	RMSE	1.27	1.64	2.39	1.84	0.91	0.52
	MBE	0.23	1.22	−1.44	−0.91	−0.82	0.29
	MAE	1.18	1.22	2.07	1.73	0.82	0.34
	%error	11.77	12.21	20.66	17.33	8.23	3.38
Douglas Co.	r^2	0.33	0.53	0.06	0.16	0.68	0.97
	RMSE	1.19	1.60	2.47	2.14	1.34	0.26
	MBE	0.20	1.17	−1.35	−1.04	−1.08	−0.11
	MAE	1.07	1.23	2.21	2.01	1.17	0.24
	%error	10.83	12.54	22.41	20.40	11.91	2.46
Total	r^2	0.28	0.47	0.13	0.29	0.80	0.93
	RMSE	1.23	1.62	2.43	1.99	1.15	0.41
	MBE	0.21	1.20	−1.40	−0.97	−0.95	0.09
	MAE	1.12	1.23	2.14	1.87	1.00	0.29
	%error	11.30	12.37	21.53	18.85	10.05	2.92

managed landscapes - predominantly a corn/soybean mosaic - the f_{RET} seasonal pattern is narrowly peaked (see their Fig. 3) due to the compressed growing season and homogeneous landcover and there is relatively little interannual variability in normalized water use. Small perturbations, due to phenological shifts in start of season or peak amplitude, therefore result in large fluctuations in the f_{RET} standardized anomalies that are only loosely related to moisture conditions. Using corn yields as a proxy indicator of agricultural drought, results in Sec. 4.5 demonstrate that a simple temporal realignment of f_{RET} to a nominal emergence date significantly improves ESI performance at the 4-km scale. The improvement is even more significant at the Landsat scale, where pure pixels of different crop types can be extracted.

Start-of-season (SOS) and/or end-of-season (EOS) metrics, derived from vegetation index (VI) time series (Reed et al., 1994) or analysis of rainfall (Agrhymet, 1996), are used in several drought indicators including the Vegetation Drought Response Index (VegDRI; Brown et al., 2008), the Water Requirement Satisfaction Index (WRSI; FAO, 1986) and the ET anomaly product (Senay et al., 2015) to better interpret apparent anomalies within the context of a changing growing season. Estimation of crop emergence date has been studied since the 1980s (Badhwar and Thompson, 1983; Badhwar and Henderson, 1985) using spectral VI data. With the launch of MODIS, global land surface phenology products are now available at 500 m spatial resolution (Friedl et al., 2002; Zhang et al., 2003). For Landsat-scale implementations, Gao et al. (2017) demonstrated that crop growth stages of emergence, peak growth and harvest can be related to remotely sensible phenological metrics developed using the STARFM fusion strategy applied to surface reflectance imagery. In particular, crop emergence date was well correlated with a "green-up" date inferred from fused vegetation index time series. This provides a capacity to improve alignment in f_{RET} curves in regions where detailed crop-specific phenological records are unavailable. However, a phenology-based correction poses challenges for operational real-time implementation, as there is a time delay involved in identification of VI inflection points.

5.3. Use of f_{RET} time series in crop simulations

Remote sensing indicators have been widely used for forecasting yield and monitoring crop condition (Becker-Reshef et al., 2010; Wardlow et al., 2012; Basso et al., 2013; Bolton and Friedl, 2013; Johnson, 2014; Zipper et al., 2016), often based on statistical regression. Recently there have been initiatives to move toward more physically based crop simulation frameworks for estimating yields (Rosenzweig et al., 2013), culminating in methods that can implemented spatially using gridded datasets (Elliott et al., 2015). Typically crop models represent seasonally varying moisture stress using simple soil water balance or ET models, but these can be susceptible to errors in soil texture and climate inputs, particularly in regions with sparse ground-based meteorological networks. Time series of f_{RET} derived from multi-scale TIR remote can be ingested into a crop simulation model as a moisture stress function, either through data assimilation or reinitialization of soil moisture at each time step. These diagnostic moisture stress data have the advantage of being independent of precipitation and soil texture inputs, and inherently incorporate irrigation supplements that are difficult to define a priori over large areas (Müller et al., 2017). The findings in Sec. 4.4 that peak f_{RET}-yield correlations for maize occur during the critical silking stage suggest that these datasets can convey spatially and temporally explicit information about crop stress down to field scales.

6. Conclusion

This study investigates correlations between yield and ESI (describing anomalies in f_{RET}, the actual-to-reference ET ratio) at the field scale over a corn/soybean production system located near Mead, NE, including both rainfed and irrigated fields. Actual ET and f_{RET} time series were generated at 30-m spatial resolution and daily time steps using a multi-satellite data fusion approach. To examine the role of crop phenology in yield-ESI correlations, the f_{RET} time series were aligned by both calendar day and by biophysically relevant dates (e.g. days since planting or emergence) prior to anomaly computation. Peak correlation of Landsat-scale f_{RET} anomalies with field-scale corn yield measurements improved from $r = 0.82$ using a calendar date alignment to $r = 0.88$ and 0.94 when f_{RET} curves are aligned on planting date and emergence date, respectively. At county scale in comparison with NASS yield survey reports for 2010–2014, adjustment of ALEXI resolution (4 km) f_{RET} to emergence date improved correlation from 0.28 to 0.80. Disaggregation of ALEXI ET to Landsat scale further facilitates crop-specific phenological alignment, and improves the yield correlations from 0.47 to 0.93 when aligning to calendar date and emergence date respectively.

The results suggest that incorporating phenological information significantly improves yield-ESI correlations. This experiment also highlights the Landsat resolution (30-m) as a beneficial scale for assessment of yield and water productivity in the U.S. Corn Belt, as pixels at this scale can differentiate between crop types and phenological stages. In contrast, pixels with coarse resolution, such as from ALEXI, carry signals with a mixture of subpixel crop types with different stages of development. This serves to decrease yield prediction capability over highly managed agricultural landscapes where the ET seasonal curve for a given crop is relatively short and peaked, and year-to-year phenological shifts in the ET time series can dominate anomaly signals developed for coarse-scale mixed pixels.

Future work will continue to develop strategies for calibrating yield-ESI functions over wider regions, given that these variables are likely to be crop-specific and regionally variable. Along with diagnostic phenological information also derived using multi-sensor data fusion, these high spatiotemporal remote sensing data sources have potential to improve yield and water productivity monitoring in data poor regions of the world. Ultimately, crop-specific f_{RET} time series could be ingested into crop simulation models for yield forecasting applicaitons.

Acknowledgement

The authors wish to thank Dr. Andy Suyker for providing yield, flux and phenology data for the Mead field sites and for comments on the manuscript in its early stage. We also thank three anonymous reviewers for providing insightful comments and suggestions, which served to substantially improve the manuscript. This work was funded in part by the NASA MEASURES program and the NASA ECOSTRESS Earth Ventures Instrument project.

References

AGRHYMET, 1996. Methodologie de suivi des zones a risque. AGRHYMET FLASH, Bulletin de Suivi de la Campagne Agricole au Sahel 2 (0/96), 2. Centre Regional AGRHYMET, B.P. 11011, Niamey, Niger.

Allen, R.G., Pereira, L.S., Raes, D., Smith, M., 1998. Crop evapotranspiration : Guidelines for computing crop water requirements. In: FAO Irrigation and Drainage Paper 56. Rome.

Allen, R.G., Tasumi, M., Morse, A., Trezza, R., Wright, J.L., Bastiaanssen, W., Kramber, W., Lorite, I.J., R, C.W., 2007. Satellite-based energy balance for mapping evapotranspiration with internalized calibration (METRIC) — applications. J. Irrig. Drain. Eng. 133, 395–406. http://dx.doi.org/10.1061/(ASCE)0733-9437(2007)133.

Anderson, M.C., Norman, J.M., Diak, G.R., Kustas, W.P., Mecikalski, J.R., 1997. A two-source time-integrated model for estimating surface fluxes using thermal infrared remote sensing. Remote Sens. Environ. 60, 195–216. http://dx.doi.org/10.1016/s0034-4257(96)00215-5.

Anderson, M.C., Norman, J.M., Mecikalski, J.R., Torn, R.D., Kustas, W.P., Basara, J.B., 2004. A multiscale remote sensing model for disaggregating regional fluxes to micrometeorological scales. J. Hydrometeorol. 5, 343–363.

Anderson, M.C., Norman, J.M., Mecikalski, J.R., Otkin, J.A., Kustas, W.P., 2007a. A climatological study of evapotranspiration and moisture stress across the continental United States based on thermal remote sensing: 1. Model formulation. J. Geophys. Res. Atmos. 112, 1–17. http://dx.doi.org/10.1029/2006JD007506.

Anderson, M.C., Norman, J.M., Mecikalski, J.R., Otkin, J.A., Kustas, W.P., 2007b. A climatological study of evapotranspiration and moisture stress across the continental United States based on thermal remote sensing: 2. Surface moisture climatology. J. Geophys. Res. Atmos. 112, 1–13. http://dx.doi.org/10.1029/2006JD007507.

Anderson, M.C., Hain, C., Wardlow, B., Pimstein, A., Mecikalski, J.R., Kustas, W.P., 2011. Evaluation of drought indices based on thermal remote sensing of evapotranspiration over the continental United States. J. Clim. 24, 2025–2044. http://dx.doi.org/10.1175/2010JCLI3812.1.

Anderson, M.C., Kustas, W.P., Alfieri, J.G., Gao, F., Hain, C., Prueger, J.H., Evett, S., Colaizzi, P., Howell, T., Chávez, J.L., 2012. Mapping daily evapotranspiration at Landsat spatial scales during the BEAREX'08 field campaign. Adv. Water Resour. 50, 162–177. http://dx.doi.org/10.1016/j.advwatres.2012.06.005.

Anderson, M.C., Hain, C., Otkin, J., Zhan, X., Mo, K., Svoboda, M., Wardlow, B., Pimstein, A., 2013. An Intercomparison of Drought Indicators based on thermal remote sensing and NLDAS-2 simulations with U.S. drought monitor classifications. J. Hydrometeorol. 14, 1035–1056. http://dx.doi.org/10.1175/JHM-D-12-0140.1.

Anderson, M.C., Zolin, C.A., Hain, C.R., Semmens, K., Tugrul Yilmaz, M., Gao, F., 2015. Comparison of satellite-derived LAI and precipitation anomalies over Brazil with a thermal infrared-based Evaporative Stress Index for 2003–2013. J. Hydrol. 526, 287–302. http://dx.doi.org/10.1016/j.jhydrol.2015.01.005.

Anderson, M.C., Zolin, C.A., Sentelhas, P.C., Hain, C.R., Semmens, K., Tugrul Yilmaz, M., Gao, F., Otkin, J.A., Tetrault, R., 2016a. The Evaporative Stress Index as an indicator of agricultural drought in Brazil: an assessment based on crop yield impacts. Remote Sens. Environ. 174, 82–99. http://dx.doi.org/10.1016/j.rse.2015.11.034.

Anderson, M.C., Hain, C.R., Jurecka, F., Trnka, M., Hlavinka, P., Dulaney, W., Otkin, J.A., Johnson, D., Gao, F., 2016b. Relationships between the evaporative stress index and winter wheat and spring barley yield anomalies in the Czech Republic. Clim. Res. 70, 215–230. http://dx.doi.org/10.3354/cr01411.

Badhwar, G.D., Henderson, K.E., 1985. Application of thematic mapper data to corn and soybean development stage estimation. Remote Sens. Environ. 17, 197–201. http://dx.doi.org/10.1016/0034-4257(85)90074-4.

Badhwar, G.D., Thompson, D.R., 1983. Estimating emergence date of spring small grains using Landsat spectral data. Agron. J. 75, 75–78.

Barr, A.G., King, K.M., Gillespie, T.J., Den Hartog, G., Neumann, H.H., 1994. A comparison of bowen ratio and eddy correlation sensible and latent heat flux measurements above deciduous forest. Bound.-Layer Meteorol. 71, 21–41. http://dx.doi.org/10.1007/BF00709218.

Basso, B., Cammarano, D., Carfagna, E., 2013. Review of Crop Yield forecasting methods and early warning systems. In: First Meet. Sci. Advis. Comm. Glob. Strateg. to Improv. Agric. Rural Stat, pp. 1–56. http://dx.doi.org/10.1017/CBO9781107415324.004.

Bastiaanssen, W.G., Ali, S., 2003. A new crop yield forecasting model based on satellite measurements applied across the Indus Basin. Agric. Ecosyst. Environ. 94, 321–340. http://dx.doi.org/10.1016/S0167-8809(02)00034-8.

Bastiaanssen, W.G.M., Pelgrum, H., Wang, J., Ma, Y., Moreno, J.F., Roerink, G.J., van der Wal, T., 1998. A remote sensing surface energy balance algorithm for land (SEBAL). J. Hydrol. 212–213, 213–229. http://dx.doi.org/10.1016/S0022-1694(98)00254-6.

Becker-Reshef, I., Vermote, E., Lindeman, M., Justice, C., 2010. A generalized regression-based model for forecasting winter wheat yields in Kansas and Ukraine using MODIS data. Remote Sens. Environ. 114, 1312–1323. http://dx.doi.org/10.1016/j.rse.2010.01.010.

Berk, A., Bernstein, L.S., Robertson, D.C., 1989. MODTRAN: A Moderate Resolution Model for LOWTRAN 7. GL-TR-89-0122. Air Force Geophysics Lab, Bedford, MA, pp. 38.

Blanken, P.D., Black, T.A., Yang, P.C., Neumann, H.H., Nesic, Z., Staebler, R., den Hartog, G., Novak, M.D., Lee, X., 1997. Energy balance and canopy conductance of a boreal aspen forest: partitioning overstory and understory components. J. Geophys. Res. 102, 28915. http://dx.doi.org/10.1029/97JD00193.

Bolton, D.K., Friedl, M.A., 2013. Forecasting crop yield using remotely sensed vegetation indices and crop phenology metrics. Agric. For. Meteorol. 173, 74–84. http://dx.doi.org/10.1016/j.agrformet.2013.01.007.

Boryan, C., Yang, Z., Mueller, R., Craig, M., 2011. Monitoring US agriculture: the US Department of Agriculture, National Agricultural Statistics Service, cropland data layer program. Geocarto Int. 26 (5), 341–358.

Brown, J.F., Wardlow, B.D., Tadesse, T., Hayes, M.J., Reed, B.C., 2008. The vegetation drought response index (VegDRI): a new integrated approach for monitoring drought stress in vegetation. GIScience Remote Sens. 45, 16–46. http://dx.doi.org/10.2747/1548-1603.45.1.16.

Cakir, R., 2004. Effect of water stress at different development stages on vegetative and reproductive growth of corn. Field Crop Res. 89, 1–16. http://dx.doi.org/10.1016/j.fcr.2004.01.005.

Cammalleri, C., Anderson, M.C., Gao, F., Hain, C.R., Kustas, W.P., 2013. A data fusion approach for mapping daily evapotranspiration at field scale. Water Resour. Res. 49, 4672–4686. http://dx.doi.org/10.1002/wrcr.20349.

Cammalleri, C., Anderson, M.C., Gao, F., Hain, C.R., Kustas, W.P., 2014. Mapping daily evapotranspiration at field scales over rainfed and irrigated agricultural areas using remote sensing data fusion. Agric. For. Meteorol. 186, 1–11. http://dx.doi.org/10.1016/j.agrformet.2013.11.001.

Carr, T., Yang, H., Ray, C., 2016. Temporal variations of water productivity in irrigated corn: an analysis of factors influencing yield and water use across Central Nebraska. PLoS One 11, 1–17. http://dx.doi.org/10.1371/journal.pone.0161944.

Claasen, M.M., Shaw, R.H., 1970. Water deficit effects on corn. II. Grain components. J. Chem. Inf. Model. 62, 652–655. http://dx.doi.org/10.1017/CBO9781107415324.004.

Cook, M., Schott, J.R., Mandel, J., Raqueno, N., 2014. Development of an operational calibration methodology for the Landsat thermal data archive and initial testing of the atmospheric compensation component of a land surface temperature (LST) product from the archive. Remote Sens. 6, 11244–11266. http://dx.doi.org/10.3390/rs61111244.

Denmead, O.T., Shaw, R.H., 1960. The effects of soil moisture stress at different stages of growth on the development and yield of corn. Agron. J. 52, 272–274. http://dx.doi.org/10.2134/agronj1960.00021962005200050010x.

Doorenbos, J., Kassam, K.H., 1979. Yield Response to Water. In: FAO Irrigation and Drainage Paper 33. Rome, FAO.

Elliott, J., Müller, C., Deryng, D., Chryssanthacopoulos, J., Boote, K.J., Büchner, M., Foster, I., Glotter, M., Heinke, J., Iizumi, T., Izaurralde, R.C., Mueller, N.D., Ray, D.K., Rosenzweig, C., Ruane, A.C., Sheffield, J., 2015. The global gridded crop model intercomparison: data and modeling protocols for phase 1 (v1.0). Geosci. Model Dev. 8, 261–277. http://dx.doi.org/10.5194/gmd-8-261-2015.

FAO, 1986. Early agrometeorological crop yield forecasting. In: Fre're, M., Popov, G.F. (Eds.), FAO Plant Production and Protection Paper No. 73. FAO, Rome, Italy.

Friedl, M.A., McIver, D.K., Hodges, J.C.F., Zhang, X., Muchoney, D., Strahler, A.H., Woodcock, C.E., Gopal, S., Schneider, A., Cooper, A., Baccini, A., Gao, F., Schaaf, C., 2002. Global land cover mapping from MODIS: algorithms and early results. Remote Sens. Environ. 83, 287–302. http://dx.doi.org/10.1016/S0034-4257(02)00078-0.

Gao, F., Masek, J., Schwaller, M., Hall, F., 2006. On the blending of the landsat and MODIS surface reflectance: predicting daily landsat surface reflectance. IEEE Trans. Geosci. Remote Sens. 44, 2207–2218. http://dx.doi.org/10.1109/TGRS.2006.872081.

Gao, F., Kustas, W.P., Anderson, M.C., 2012a. A data mining approach for sharpening thermal satellite imagery over land. Remote Sens. 4, 3287–3319. http://dx.doi.org/10.3390/rs4113287.

Gao, F., Anderson, M.C., Kustas, W.P., Wang, Y., 2012b. Simple method for retrieving leaf area index from Landsat using MODIS leaf area index products as reference. J. Appl. Remote. Sens. 6, 63554. http://dx.doi.org/10.1117/1.JRS.6.063554.

Gao, F., Hilker, T., Zhu, X., Anderson, M.A., Masek, J., Wang, P., Yang, Y., 2015. Fusing Landsat and MODIS data for vegetation monitoring. IEEE Geosci. Remote Sens. Mag. 3 (3), 47–60. http://dx.doi.org/10.1109/MGRS.2015.2434351.

Gao, F., Anderson, M.C., Zhang, X., Yang, Z., Alfieri, J.G., Kustas, W.P., Mueller, R., Johnson, D.M., Prueger, J.H., 2017. Toward mapping crop progress at field scales through fusion of Landsat and MODIS imagery. Remote Sens. Environ. 188, 9–25. http://dx.doi.org/10.1016/j.rse.2016.11.004.

Hansen, M.C., Defries, R.S., Townshend, J.R.G., Sohlberg, R., 2000. Global land cover classification at 1 km spatial resolution using a classification tree approach. Int. J.

Remote Sens. http://dx.doi.org/10.1080/014311600210209.
Hanway, J.J., 1966. How a corn plant develops. In: Spec. Rep. 48. Iowa State Univ., Coop. Ext. Serv., Ames, Iowa.
Homer, C.G., Dewitz, J.A., Yang, L., Jin, S., Danielson, P., Xian, G., Coulston, J., Herold, N.D., Wickham, J.D., Megown, K., 2015. Completion of the 2011 National Land Cover Database for the conterminous United States-representing a decade of land cover change information. Photogramm. Eng. Remote. Sens. 81, 345–354. http://dx.doi.org/10.14358/PERS.81.5.345.
Hsiao, T.C., Fereres, E., Acevedo, E., Henderson, D.W., 1976. Water Stress and Dynamics of Growth and Yield of Crop Plants. Water and plant life. Springer, Berlin Heidelberg, pp. 281–305. http://dx.doi.org/10.1007/978-3-642-66429-8_18.
Jensen, M., 1968. Water Consumption by Agricultural Plants. Water Deficits and Plant Growth. Academic Press, New York.
Johnson, D.M., 2014. An assessment of pre- and within-season remotely sensed variables for forecasting corn and soybean yields in the United States. Remote Sens. Environ. 141, 116–128. http://dx.doi.org/10.1016/j.rse.2013.10.027.
Kalma, J.D., McVicar, T.R., McCabe, M.F., 2008. Estimating land surface evaporation: a review of methods using remotely sensed surface temperature data. Surv. Geophys. 29, 421–469. http://dx.doi.org/10.1007/s10712-008-9037-z.
Kjaersgaard, J., Allen, R., Irmak, A., 2011. Improved methods for estimating monthly and growing season ET using METRIC applied to moderate resolution satellite imagery. Hydrol. Process. 25, 4028–4036. http://dx.doi.org/10.1002/hyp.8394.
Kustas, W., Anderson, M., 2009. Advances in thermal infrared remote sensing for land surface modeling. Agric. For. Meteorol. 149, 2071–2081. http://dx.doi.org/10.1016/j.agrformet.2009.05.016.
Kustas, W.P., Norman, J.M., 1997. A two-source approach for estimating turbulent fluxes using multiple angle thermal infrared observations. Water Resour. Res. 33, 1495–1508. http://dx.doi.org/10.1029/97WR00704.
Kustas, W.P., Norman, J.M., 1999. Evaluation of soil and vegetation heat flux predictions using a simple two-source model with radiometric temperatures for partial canopy cover. Agric. For. Meteorol. 94, 13–29. http://dx.doi.org/10.1016/S0168-1923(99)00005-2.
Masek, J.G., Vermote, E.F., Saleous, N.E., Wolfe, R., Hall, F.G., Huemmrich, K.F., Gao, F., Kutler, J., Lim, T.K., 2006. A landsat surface reflectance dataset for North America, 1990-2000. IEEE Geosci. Remote Sens. Lett. 3, 68–72. http://dx.doi.org/10.1109/LGRS.2005.857030.
McMaster, G.S., 2004. Simulating crop phenology. In: 4th International Crop Science Congress. Brisbane, Australia, September 27-October 1 2004.
McNaughton, K.G., Spriggs, T.W., 1986. A mixed-layer model for regional evaporation. Bound.-Layer Meteorol. 34, 243–262. http://dx.doi.org/10.1007/BF00122381.
Mishra, V., Cruise, J.F., Mecikalski, J.R., Hain, C.R., Anderson, M.C., 2013. A remote-sensing driven tool for estimating crop stress and yields. J. Remote Sens. 5, 3331–3356.
Mkhabela, M., Bullock, P., Gervais, M., Finlay, G., Sapirstein, H., 2010. Assessing indicators of agricultural drought impacts on spring wheat yield and quality on the Canadian prairies. Agric. For. Meteorol. 150, 399–410.
Mladenova, I.E., Bolten, J.D., Crow, W.T., Anderson, M.C., Hain, C.R., Johnson, D.M., Mueller, R., 2017. Intercomparison of soil moisture, evaporative stress, and vegetation indices for estimating corn and soybean yields over the U.S. IEEE J. Sel. Top. Appl. Earth Obs. Remote Sens. 10, 1328–1343. http://dx.doi.org/10.1109/JSTARS.2016.2639338.
Müller, C., Elliott, J., Chryssanthacopoulos, J., Arneth, A., Balkovic, J., Ciais, P., Deryng, D., Folberth, C., Glotter, M., Hoek, S., Iizumi, T., Izaurralde, R.C., Jones, C., Khabarov, N., Lawrence, P., Liu, W., Olin, S., Pugh, T.A.M., Ray, D.K., Reddy, A., Rosenzweig, C., Ruane, A.C., Sakurai, G., Schmid, E., Skalsky, R., Song, C.X., Wang, X., De Wit, A., Yang, H., 2017. Global gridded crop model evaluation: benchmarking, skills, deficiencies and implications. Geosci. Model Dev. 10, 1403–1422. http://dx.doi.org/10.5194/gmd-10-1403-2017.
Myneni, R., 2014. 4-day MODIS LAI/FPAR – MCD15A3. In: NASA Land Processes Distributed Active Archive Center (LP DAAC). South Dakota, USGS/Earth Resources Observation and Science (EROS) Center, Sioux Falls.
NASS CDL, 2017. http://www.nass.usda.gov/Research_and_Science/Cropland/SARS1a.php, Accessed date: 30 March 2017.
NASS CPR, 2017. http://www.nass.usda.gov/Publications/National_Crop_Progress/, Accessed date: 30 March 2017.
Nellis, M.D., Price, K.P., Rundquist, D., 2009. Remote sensing of cropland agriculture. In: The SAGE Handbook of Remote Sensing, pp. 1–27. http://dx.doi.org/10.4135/978-1-8570-2105-9.n26.
NeSmith, D.S., Ritchie, J.T., 1992. Effects of soil water-deficits during tassel emergence on development and yield component of maize (Zea mays). Field Crop Res. 28, 251–256. http://dx.doi.org/10.1016/0378-4290(92)90044-A.
Norman, J.M., Kustas, W.P., Humes, K.S., 1995. Source approach for estimating soil and vegetation energy fluxes in observations of directional radiometric surface temperature. Agric. For. Meteorol. 77, 263–293. http://dx.doi.org/10.1016/0168-1923(95)02265-Y.
Norman, J.M., Anderson, M.C., Kustas, W.P., French, A.N., Mecikalski, J., Torn, R., Diak, G.R., Schmugge, T.J., Tanner, B.C.W., 2003. Remote sensing of surface energy fluxes at 10^1-m pixel resolutions. Water Resour. Res. 39 n/a-n/a. https://doi.org/10.1029/2002WR001775.
Otkin, J.A., Anderson, M.C., Hain, C., Svoboda, M., 2013. Examining rapid onset drought development using the thermal infrared–based evaporative stress index. J. Hydrometeorol. 131101141751009. http://dx.doi.org/10.1175/JHM-D-13-0110.1.
Otkin, J.A., Anderson, M.C., Hain, C., Svoboda, M., 2014. Examining the relationship between drought development and rapid changes in the evaporative stress index. J. Hydrometeorol. 15, 938–956. http://dx.doi.org/10.1175/JHM-D-13-0110.1.
Otkin, J.A., Anderson, M.C., Hain, C., Svoboda, M., 2015. Using temporal changes in drought indices to generate probabilistic drought intensification forecasts. J. Hydrometeorol. 16, 88–105. http://dx.doi.org/10.1175/JHM-D-14-0064.1.
Otkin, J.A., Anderson, M.C., Hain, C., Svoboda, M., Johnson, D., Mueller, R., Tadesse, T., Wardlow, B., Brown, J., 2016. Assessing the evolution of soil moisture and vegetation conditions during the 2012 United States flash drought. Agric. For. Meteorol. 218–219, 230–242. http://dx.doi.org/10.1016/j.agrformet.2015.12.065.
Otkin, J.A., Svoboda, M., Hunt, E., Ford, T., Anderson, M., Hain, C., Basara, J., 2018. Flash Droughts: A Review and Assessment of the Challenges Imposed by Rapid Onset Droughts in the United States. Bull. Am. Meteorol, Soc (in press).
Reed, B.C., Brown, J.F., VanderZee, D., Loveland, T.R., Merchant, J.W., Ohlen, D.O., 1994. Measuring phenological variability from satellite imagery. J. Veg. Sci. 5, 703–714. http://dx.doi.org/10.2307/3235884.
Rosenzweig, C., Jones, J.W., Hatfield, J.L., Ruane, A.C., Boote, K.J., Thorburn, P., Antle, J.M., Nelson, G.C., Porter, C., Janssen, S., Asseng, S., Basso, B., Ewert, F., Wallach, D., Baigorria, G., Winter, J.M., 2013. The agricultural model intercomparison and improvement project (AgMIP): protocols and pilot studies. (special issue: agricultural prediction using climate model ensembles). Agric. For. Meteorol. 170, 166–182. http://dx.doi.org/10.1016/j.agrformet.2012.09.011.
Saha, S., Moorthi, S., Wu, X., Wang, J., Nadiga, S., Behringer, D., Hou, Y., Chuang, H., Iredell, M., Ek, M., 2014. The NCEP climate forecast system version 2. J. Clim. 27, 2185–2208.
Schaaf, C.L.B., Liu, J., Gao, F., Strahler, A.H., 2011. MODIS Albedo and reflectance anisotropy products from Aqua and Terra. In: Ramachandran, B., Justice, C., Abrams, M. (Eds.), Land Remote Sensing and Global Environmental Change: NASA's Earth Observing Systemand the Science of ASTER andMODIS, Remote Sensing and Digital Image Pro-cessing Series. vol. 11 Springer-Cerlag (873 pp).
Seguin, B., Becker, F., Phulpin, T., Gu, X.F., Guyot, G., Kerr, Y., King, C., Lagouarde, J.P., Ottlé, C., Stoll, M.P., Tabbagh, A., 1999. IRSUTE: a mini satellite for land surface flux estimation from the local field to the regional scale. Remote Sens. Environ. 68, 357–369.
Semmens, K.A., Anderson, M.C., Kustas, W.P., Gao, F., Alfieri, J.G., McKee, L., Prueger, J.H., Hain, C.R., Cammalleri, C., Yang, Y., Xia, T., Sanchez, L., Mar Alsina, M., Vélez, M., 2015. Monitoring daily evapotranspiration over two California vineyards using Landsat 8 in a multi-sensor data fusion approach. Remote Sens. Environ. http://dx.doi.org/10.1016/j.rse.2015.10.025.
Senay, G.B., Bohms, S., Singh, R.K., Gowda, P.H., Velpuri, N.M., Alemu, H., Verdin, J.P., 2013. Operational evapotranspiration mapping using remote sensing and weather datasets: a new parameterization for the SSEB approach. J. Am. Water Resour. Assoc. 49, 577–591. http://dx.doi.org/10.1111/jawr.12057.
Senay, G.B., Velpuri, N.M., Bohms, S., Budde, M., Young, C., Rowland, J., Verdin, J.P., 2015. Drought monitoring and assessment: remote sensing and modeling approaches for the famine early warning systems network. In: USGS Staff – Published Research, pp. 858.
Steduto, P., Hsiao, T.C., Fereres, E., Raes, D., 2012. Crop yield response to water. In: Fao Irrigation and Drainage Paper Issn. Roma.
Sun, L., Anderson, M.C., Gao, F., Hain, C.R., Alfieri, J.G., Sharifi, A., McCarty, G.W., Yang, Y., Yang, Y., Kustas, W.P., McKee, L., 2017. Investigating water use over the Choptank River Watershed using a multi-satellite data fusion approach. Water Resour. Res. 53, 5298–5319. http://dx.doi.org/10.1002/2017WR020700.
Suyker, A.E., Verma, S.B., 2009. Evapotranspiration of irrigated and rainfed maize-soybean cropping systems. Agric. For. Meteorol. 149, 443–452. http://dx.doi.org/10.1016/j.agrformet.2008.09.010.
Suyker, A.E., Verma, S.B., Burba, G.G., Arkebauer, T.J., Walters, D.T., Hubbard, K.G., 2004. Growing season carbon dioxide exchange in irrigated and rainfed maize. Agric. For. Meteorol. 124, 1–13. http://dx.doi.org/10.1016/j.agrformet.2004.01.011.
Svoboda, M., LeComte, D., Hayes, M., Heim, R., Gleason, K., Angel, J., Rippey, B., Tinker, R., Palecki, M., Stooksbury, D., Miskus, D., Stephens, S., 2002. The drought monitor. Bull. Am. Meteorol. Soc. 83, 1181–1190.
Tadesse, T., Senay, G.B., Berhan, G., Regassa, T., Beyene, S., 2015. Evaluating a satellite-based seasonal evapotranspiration product and identifying its relationship with other satellite-derived products and crop yield: A case study for Ethiopia. Int. J. Appl. Earth Obs. Geoinf. 40, 39–54. http://dx.doi.org/10.1016/j.jag.2015.03.006.
Twine, T.E., Kustas, W.P., Norman, J.M., Cook, D.R., Houser, P.R., Meyers, T.P., Prueger, J.H., Wesley, M.L., 2000. Correcting eddy covariance flux underestimates over grassland. Agric. For. Meteorol. 103, 279–300. http://dx.doi.org/10.1016/S0168-1923(00)00123-4.
Van Niel, T.G., McVicar, T.R., Roderick, M.L., Van Dijk, A.I.J.M., Renzullo, L.J., Van Gorsel, E., 2011. Correcting for systematic error in satellite-derived latent heat flux due to assumptions in temporal scaling: assessment from flux tower observations. J. Hydrol. 409, 140–148. http://dx.doi.org/10.1016/j.jhydrol.2011.08.011.
Van Niel, T.G., McVicar, T.R., Roderick, M.L., Van Dijk, A.I.J.M., Beringer, J., Hutley, L.B., Van Gorsel, E., 2012. Upscaling latent heat flux for thermal remote sensing studies: comparison of alternative approaches and correction of bias. J. Hydrol. 468–469, 35–46. http://dx.doi.org/10.1016/j.jhydrol.2012.08.005.
Wan, Z., 2014. MODIS land surface temperature product – MOD11_L2 V005. In: NASA Land Processes Distributed Active Archive Center (LP DAAC). USGS/Earth Resources Observation and Science (EROS) Center, Sioux Falls, South Dakota.
Wang, K., Dickinson, R.E., 2012. A review of global terrestrial evapotranspiration: observation, modelling, climatology, and climatic variability. Rev. Geophys. 50, 1–54.
Wardlow, B.D., Anderson, M.C., Verdin, J.P. (Eds.), 2012. Remote Sensing of Drought: Innovative Monitoring Approaches. CRC Press. Taylor and Francis, Boca Raton, FL.
Willmott, C., 1982. Some comments on the evaluation of model performance. Bull. Am. Meteorol. Soc. 63, 1309–1313.
Willmott, C.J., Matsuura, K., 2005. Advantages of the mean absolute error (MAE) over the root mean square error (RMSE) in assessing average model performance. Clim. Res. 30, 79–82. http://dx.doi.org/10.3354/cr030079.

Wilson, J.H., 1968. Water relations of maize. Effects of severe soil moisture stress imposed at different stages of growth on grain yields of maize. Rhod. J. Agric. Res. 6, 103–105.
Wilson, K., 2002. Energy balance closure at FLUXNET sites. Agric. For. Meteorol. 113, 223–243. http://dx.doi.org/10.1016/S0168-1923(02)00109-0.
Yang, Y., Anderson, M.C., Gao, F., Hain, C.R., Kustas, W., Meyers, T., Crow, W., Finocchiaro, R., Otkin, J.A., Sun, L., Yang, Y., 2017a. Impact of tile drainage on evapotranspiration in South Dakota, USA, based on high spatiotemporal resolution evapotranspiration time series from a multisatellite data fusion system. IEEE J. Sel. Top. Appl. Earth Obs. Remote Sens. http://dx.doi.org/10.1109/JSTARS.2017.2680411.
Yang, Y., Anderson, M.C., Gao, F., Hain, C.R., Semmens, K.A., Kustas, W.P., Noormets, A., Wynne, R.H., Thomas, V.A., Sun, G., 2017b. Daily Landsat-scale evapotranspiration estimation over a forested landscape in North Carolina, USA using multi-satellite data fusion. Hydrol. Earth Syst. Sci. Discuss. 1–45. http://dx.doi.org/10.5194/hess-2016-198.
Zhang, X., Friedl, M.A., Schaaf, C.B., Strahler, A.H., Hodges, J.C.F., Gao, F., Reed, B.C., Huete, A., 2003. Monitoring vegetation phenology using MODIS. Remote Sens. Environ. 84, 471–475. http://dx.doi.org/10.1016/S0034-4257(02)00135-9.
Zipper, S.C., Qiu, J., Kucharik, C.J., 2016. Drought effects on US maize and soybean production: spatiotemporal patterns and historical changes. Environ. Res. Lett. 11, 094021. http://dx.doi.org/10.1088/1748-9326/11/9/094021.